Journal of Materials Chemistry C

ROYAL SOCIETY OF CHEMISTRY

REVIEW

View Article Online
View Journal | View Issue

Cite this: *J. Mater. Chem. C*, 2024, **12**, 14729

An overview of Joule heating in energy storage materials and applications

Jiahui Yuan, Yizi Zhang, Fuzhou Chen and Zhengrong Gu *

Received 27th April 2024,
Accepted 6th August 2024

DOI: 10.1039/d4tc01736f

rsc.li/materials-c

Joule heating, a fundamental process converting electrical energy into heat, can be used to prepare many materials for energy storage. This review explores the multifaceted role of Joule heating. The application of Joule heating in the preparation of graphene, graphene oxide fibers, metastable 2D materials, boron carbon nitride and carbon nanotubes, as well as optimization and regeneration of energy storage materials, is summarized. Also, we focus on various energy storage systems such as batteries, supercapacitors, electrode material recycling, solid-state electrolytes and current collectors. Additionally, this paper discusses the applications, principles, advantages, and challenges of Joule heating, aimed at enhancing the overall performance and longevity of energy storage materials. By amalgamating crucial insights from existing research, this review aims to comprehensively understand the role and significance of Joule heating in energy storage technologies for energy material applications.

1. Introduction

With the accelerated depletion of chemical energy resources and the increasing global energy demand, the global energy landscape is undergoing a significant transformation, leading to a growing demand for renewable energy. In this context, developing more advanced and efficient energy storage technologies has become imperative, with renewable energy storage systems emerging as a research focus. Traditional synthesis techniques for energy storage materials, such as the hydrothermal method, chemical vapor deposition (CVD), and high-temperature calcination annealing, each have their advantages and limitations. However, these methods usually require long heating and cooling processes, extended reaction durations, and post-synthesis separation and drying steps. Recently, techniques such as microwave irradiation (MW),[1,2] laser ablation (LA),[3,4] magnetic induction heating (MIH),[5] and Joule heating (JH)[6,7] have gained popularity among researchers due to their extremely high synthesis efficiency and energy utilization rates. Joule heating technology, which includes high-temperature shock (HTS)[8] and flash Joule heating (FJH) methods,[9] can shorten the reaction process to seconds or even milliseconds and eliminate the need for post-synthesis separation,[9] achieving ultrafast synthesis of energy storage materials. Joule heating (JH) technology, as an emerging method in energy storage applications, has garnered considerable attention. Currently, JH is not only widely used in the synthesis of various carbon

Department of Agricultural and Biosystems Engineering, South Dakota State University, Brookings, SD, 57007, USA. E-mail: Zhengrong.Gu@sdstate.edu

Jiahui Yuan

Jiahui Yuan received his BS degree from South China Agricultural University in 2018. Currently, he is a PhD student in the Department of Agricultural and Biosystems Engineering at South Dakota State University. His research interest is focused on supercapacitors and batteries.

Yizi Zhang

Yizi Zhang received her BS degree from South China Agricultural University in 2018. She received her master's degree in chemical engineering from Wuyi University in 2022. Now, she is a PhD student in the Department of Agricultural and Biosystems Engineering at South Dakota State University.

materials and two-dimensional nanomaterials such as graphene, turbostratic boron nitride, and molybdenum sulfide, but also successfully applied in areas such as high-entropy oxides, high-entropy alloys,[10] solid-state electrolytes' synthesis and electrode material recycling. The JH technique evolves towards broader material synthesis directions and demonstrates enormous potential.

Currently, there is still no literature providing a review of the application of JH in the field of energy storage. In this review, the current research status of the progress of Joule heating in energy storage was summarized, which discusses the process methods, material compositions, and properties of different JH technique prepared materials. Also, this review focuses on the current research status in energy storage applications such as battery electrodes, supercapacitors, electrode material recycling, solid-state electrolytes, and current collector treatment. Moreover, this review emphasizes the advantages and importance of JH technology in the field of energy storage. Future application prospects and challenges for future development were predicted.

1.1. Joule effect

The Joule effect, named after the British physicist James Prescott Joule (1818–1889), was formally proposed in the mid-19th century. Joule immersed a conductor in water of known mass and passed an electric current through it. While ensuring uniform water temperature, he recorded the time and temperature changes.[11] Through repeated experiments and data analysis, Joule successfully derived the relationship between current and heat generated. Joule submitted his significant findings in the form of a paper to the Royal Society of London,[12] which indicated the relationship between the heat emitted by a conductor and the current, resistance, and duration of current flow, known as Joule's Law, expressed by the formula $Q = I^2RT$, where Q represents the heat in Joules (J), I represents the current in amperes (A), R represents the resistance in ohms (Ω), and t represents the duration of current flow in seconds (s). The Joule effect reveals that electrical energy can be converted into heat energy, constituting one of the foundational principles of thermodynamics, and holds significant importance in energy conversion, industrial production, scientific research, and other fields.

1.2. Disruptive potential of Joule heating technology

However, as a commonly encountered phenomenon in electrical systems, the Joule effect is often considered an undesirable byproduct.[13] In conductors such as wires, batteries, or supercapacitors, the electrical resistance within the materials leads to the generation of heat when current passes through, resulting in the conversion of some electrical energy into thermal energy.[14] This not only causes energy wastage but also adversely affects the lifespan and performance of energy storage components and may even lead to safety incidents such as spontaneous combustion.

Despite these drawbacks, due to the rapid heat generation, high efficiency, and minimal pollution associated with the Joule effect, this heat can be widely utilized across various fields, including resistance heating (*e.g.*, electric furnaces, soldering irons, rice cookers, and electric irons), resistance welding, metal smelting, medical therapy, and more. In the field of materials science and engineering, JH technology, as an efficient heating method, particularly under high-temperature reaction conditions, offers the advantage of creating high-temperature environments and rapid heating, which is significant for the synthesis of certain materials. Over the past few decades, the application of JH in materials preparation has made significant progress and demonstrated potential in multiple domains.[15] For instance, in recent decades, JH has been employed in the synthesis of ceramic materials,[16–18] metal powder metallurgy,[19] nanoparticle fabrication,[20] and other fields.[21–23] JH technology provides rapid, uniform, and precisely controllable heating effects, contributing to the improvement of material performance and structure, thereby paving the way for a novel approach to material synthesis.

JH technology, due to its independence from the use of furnaces, solvents, and reaction gases, circumvents the common issues of energy consumption and environmental pollution in traditional processes.[8,9] It represents a disruptive new approach to conventional muffle and tube furnace calcination methods. JH enables extremely rapid heating and cooling rates

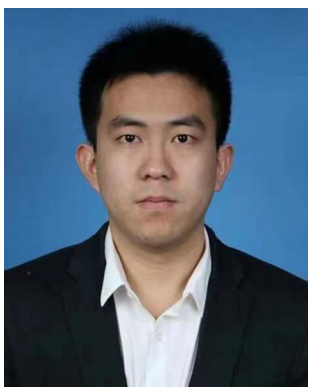

Fuzhou Chen

Dr. Fuzhou Chen received his BS degree in Physics from Lanzhou University in 2016. He received his PhD degree from Shandong University in 2021. His current research focuses on the synthesis of transition metal nanomaterials and their application in energy conversion and storage fields.

Zhengrong Gu

Dr. Zhengrong Gu received his PhD degree in Chemical Engineering from Iowa State University. Dr. Gu is a professor in the Department of Agricultural and Biosystems Engineering at South Dakota State University. Dr. Gu's research interest focuses on synthesis of functional carbon nanomaterials for applications, such as energy storage, catalysis, separation, biosensing and biomedical therapy.

(typically reaching several tens to hundreds of degrees Celsius per second) and high target temperatures,[24] thereby significantly reducing the duration of the reaction process (usually <10 s) and achieving energy efficiency several orders of magnitude higher than traditional heating methods. Importantly, the ultra-short heating and cooling processes avoid unnecessary thermal effects, such as material oxidation,[25] uneven structural changes due to temperature gradients, and particle sintering.[24] Furthermore, by adjusting the heating time of JH, the size of nanoparticles can be controlled, which plays a crucial role in controlling the functional activity of materials. For example, by reducing the JH time from 10 seconds to 1 second, Xia *et al.* achieved size modulation of Pt nanoparticles, yielding ultrafine nanoparticles of 1.5 nm, with the potential for further size reduction by further shortening the heating time.[24]

1.3. Two unique approaches

JH technology can be roughly classified into two types based on the heating method employed: one involves coating or sandwiching the material to be processed between thin carbon strips or carbon fabrics. When electric current passes through, the presence of resistance leads to the conversion of electrical energy into heat. The temperature of the conductor material rapidly increases, and the heat is then transferred to the material to be processed *via* thermal radiation, thereby facilitating rapid thermal treatment of the material.[8,26] For instance, by sandwiching ceramic precursor powder compacts between two Joule-heated carbon tapes, the resistance heating of the thin carbon tape can provide temperatures as high as $\sim$3000 °C. During the reaction, both heating and cooling rates are very high, enabling ultrafast sintering of ceramic materials within approximately 10 seconds.[16] Another one is Flash Joule Heating (FJH), where the material to be processed is directly used as the conductor material (typically requiring the incorporation of a certain proportion of carbon black to ensure conductivity). Through the discharge of a large capacitor in milliseconds, the material to be processed can instantly reach ultra-high temperatures, allowing the thermal treatment process to be completed in an extremely short time. During the FJH current discharge, most of the heat is emitted in the form of blackbody radiation flashes,[27] so the FJH process is typically accompanied by very bright flashes. The instantaneous temperature of the sample can be calculated using the blackbody radiation equation:[28]

$$B_\lambda(\lambda, T) = \gamma \varepsilon_{\text{gray}} \frac{2hc^2}{\lambda^5} \frac{1}{e^{hc/\lambda k_B T} - 1}$$

where $\varepsilon_{\text{gray}}$ represents the constant emissivity, T denotes the temperature, h denotes the Planck constant, k_B denotes the Boltzmann constant, c denotes the speed of light, λ denotes the wavelength, and γ denotes the fitting constant. In a typical case, the carbon source is gently compressed between two electrodes inside a quartz tube, with graphite spacers or copper wool plugs separating the carbon source and electrodes. The compression force is controlled using a modified small vice at both ends, maintaining the sample resistance between 1 and 1000 Ω. A capacitor bank with a total capacitance of 0.22 F serves as the power source, and the discharge time is controlled using mechanical relays with a programmable millisecond-level delay time. The carbon source reaches temperatures >3000 K in less than 100 milliseconds and successfully converts into flash graphene (FG).[9]

2. Joule heating materials

2.1. Graphene

In light of graphene's remarkable properties including mechanical exfoliation,[29,30] chemical vapor deposition (CVD),[31–33] and chemical oxidation–reduction methods,[34,35] graphene has been widely applied in various fields, showcasing remarkable performance.[36] Although significant advancements have been made in graphene production technologies, large-scale production of graphene still faces numerous challenges, primarily due to the scale limitations and high production costs. On the one hand, the synthesis of graphene oxide (GO), as a precursor for graphene production, poses a significant barrier to its large-scale commercialization. Besides, the commonly used Hummers' method[37] and modified Hummer's methods[38,39] suffer from high costs, generation of chemical waste, and poor environmental friendliness during GO synthesis. Although the CVD method is utilized for synthesizing high-quality graphene,[40] its high cost and low yield continue to impede its commercialization. The FJH technology provides an innovative solution to the challenges of traditional methods by enabling rapid, cost-effective, and environmentally friendly graphene synthesis through direct electrical heating. FJH technology heats materials directly with electric current, rapidly reaching the required high temperatures in an extremely short duration.[9] Compared to traditional methods such as CVD or chemical oxidation–reduction methods, FJH not only significantly reduces energy consumption but also avoids the use of harmful chemicals, effectively reducing the generation of chemical waste. Furthermore, FJH allows for more precise control of temperature and heating duration, which helps enhance the quality of graphene and improves its electrochemical properties.

The FJH technology is widely used in the preparation of graphene.[9] Luong *et al.* proposed an innovative technique-FJH to enhance the production efficiency of graphene and facilitate its large-scale commercialization.[9] This technique utilizes inexpensive carbon sources such as coal, petroleum coke, biochar, carbon black, food waste, rubber tires, and mixed plastic waste for rapid JH. It does not require a furnace, solvents, or reaction gases and can produce gram-scale quantities of graphene in an extremely short time at high temperatures (>3000 K) (Fig. 1a). The product of this technique is termed flash graphene (FG), exhibiting disordered stacking between graphene layers (Fig. 1b–d). FG achieves yields as high as 80–90% with carbon content sources such as carbon black, anthracite coal, or calcined coke, with purity exceeding 99%, and no purification

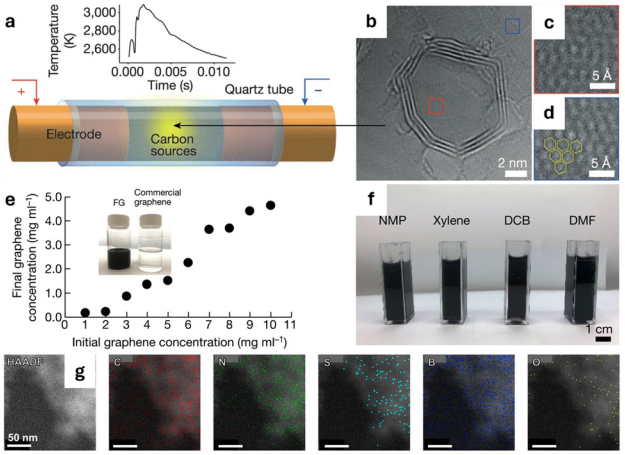

Fig. 1 (a) The schematic diagram of the FJH process, and temperature rise curve with time during flashing. (b)–(d) The HR-TEM image of FG from carbon black on top of a single layer of coffee-derived FG. (e) Dispersion of FG in water–pluronic (F-127) solution (1%). The photograph shows the supernatant after centrifugation of 4 g l^{-1} of CB-FG and 10 g l^{-1} of a commercial sample. (f) The dispersion of FG in various organic solvents at 5 g l^{-1}. Reproduced with permission from ref. 9. Copyright 2020 Springer Nature. (g) STEM image and corresponding elemental distribution of boron (B), nitrogen (N), and sulfur (S) codoped flash graphene. Reproduced with permission from ref. 6. Copyright 2022 American Chemical Society.

steps required, significantly enhancing production efficiency. Due to its turbostratic structure allowing for effective exfoliation, FG boasts advantages including high dispersibility and low interlayer attraction. Thus, FG demonstrates superior dispersibility compared to commercial graphene, dispersing uniformly in water and organic solvents (Fig. 1e and f). Additionally, it boasts a low energy cost for synthesizing FG, amounting to approximately 7.2 kilojoules per gram. The outstanding production efficiency and low production costs will significantly propel applications of FG in energy storage, catalysis, large-scale construction composite materials, and other fields.

It has been demonstrated that many materials can be effectively converted into flash graphene through FJH. The FJH method for producing graphene can utilize not only high-carbon materials such as wood charcoal, carbon black, and anthracite coal[41] but also various low-value carbon sources and even waste carbon sources. These include pine bark, potato peels, coconut shells, coffee grounds, pistachio shells, sugarcane bagasse, as well as bio-waste[42] and rubber waste.[43] Even plastic waste[44] and the valueless pyrolysis ash generated from the pyrolysis of plastic waste[45] can also be effortlessly transformed into high-purity flash graphene through the FJH method. Plastic waste pollution stands as a pressing environmental concern[46] and physical recycling requires significant human and material resources.[47,48] Therefore, FJH unquestionably presents a novel approach to tackling plastic waste pollution and fostering sustainable development.

By employing the FJH technique, the production yield of FG has been increased to 1 ton per day. Building upon this achievement, Chen *et al.* employed the FJH technique without catalysts or solvents to directly synthesize seven types of heteroatom-doped FG in milliseconds.[6] These include single-element doping (boron, nitrogen, oxygen, phosphorus, sulfur), dual-element co-doping (boron and nitrogen), and triple-element co-doping (boron, nitrogen, and sulfur) FG. High-quality heteroatom-doped FG synthesis was achieved using low-cost dopants such as elements, oxides, and organic compounds (Fig. 1g). The heteroatom-doped FG displayed exceptional graphene quality and enhanced electronic structure, featuring turbostraticity, expanded interlayer spacing, and remarkable dispersibility. Further testing was conducted on the application performance of different heteroatom-doped flash graphene in electrochemical oxygen reduction reactions (ORRs) and lithium metal batteries. The results demonstrated that sulfur-doped FG exhibited the best oxygen reduction reaction performance, while nitrogen-doped FG showed a smaller nucleation overpotential compared to copper or undoped FG. Additionally, the synthesized doped FG had low energy costs, ranging from 1.2 to 10.7 kJ g^{-1}, making it suitable for low-cost large-scale production. Therefore, the FJH method provides a feasible approach for low-cost and efficient preparation of doped graphene, with significant application prospects and scalability.

Compared to other graphene synthesis methods, FJH offers outstanding advantages. The advantages and limitations of FJH in comparison to other methods are summarized in Table 1.

2.2. Graphene oxide fibers (GOFs)

During the preparation process of graphene oxide fibers (GOFs), inevitably, some defect structures are involved, such as oxygen functional groups (*e.g.*, carboxyl, hydroxyl, epoxide) and extensive disruption of the sp^2-bonding network,[51,52] which significantly affect the performance of graphene. These defect structures impair the electrical transport properties within the graphene plane, interrupt electron hopping conduction in disordered regions, and hinder the Schottky barrier tunneling effect at contact points,[53] leading to a decrease in graphene conductivity. Currently, the primary approaches for repairing defects include chemical reduction[54] and heat treatment.[55] Traditional methods often face multiple challenges when repairing defects such as high temperatures required for extended periods, leading to high energy consumption and difficulties in precisely controlling the microstructure due to prolonged cooling processes. Moreover, it is challenging for these methods to repair existing defects without introducing new ones, such as mild reduction of GO or structural damage.[56] JH offers a solution by instantaneously generating temperatures above 2000 °C through electric current, which helps to quickly repair defects in GOFs.[57] Additionally, the direction of the current can control the texture of the graphene oxide, significantly impacting the transmission properties along the fiber axis. Therefore, JH not only provides a rapid processing solution but also is environmentally friendly and energy-efficient, and significantly enhances the electrical conductivity and mechanical strength of GOFs.

Table 1 Comparison of advantages and limitations of different synthesis methods for Graphene

Method	Advantages	Limitations	Ref.
FJH	1. Utilizes electric current to directly convert material resistance into heat, achieving high efficiency and very rapid synthesis, completing the process in a very short time. 2. Wide range of carbon sources, including coal, biomass, and even plastic waste. 3. The synthesized FG has good dispersibility and low interlayer attraction, resulting in better dispersibility than commercial graphene. 4. High quality and purity of FG.	1. Requires precise control of current and temperature to obtain high-quality graphene.	9
CVD	1. Can produce high-quality single or few-layer graphene. 2. Can directly grow graphene films on metal substrates. 3. Suitable for large-area graphene film production.	1. High cost, requires high purity gases and expensive metal substrates. 2. High environmental requirements for the process, needing high vacuum or high temperature conditions.	49
Chemical exfoliation	1. Does not require special equipment or high-temperature reactions. 2. Easy to achieve large-scale production.	1. Uses strong oxidizers and strong reducing agents, requiring attention to safety. 2. The oxidation and reduction process can lead to defects and oxygen-containing groups, reducing the electrical conductivity and mechanical strength of graphene. 3. Produces toxic chemical residues and large amounts of waste.	50
Mechanical exfoliation	1. Produces high-purity graphene. 2. Does not require chemical reagents.	1. Easily causes material fragmentation, creating defects within graphene flakes and affecting the product's electrical and mechanical properties. 2. The graphene produced has very low yield and poor dispersion in solvents. 3. Difficult to achieve large-scale production.	29

Noh *et al.* proposed a method based on JH to effectively repair defects in GOFs (Fig. 2a).[57] This method enables the control of heating temperature by regulating the input current, allowing rapid, environmentally friendly, and energy-efficient restoration of the sp^2 lattice structure within GOFs. It also enables precise control over the level of sp^2 restoration and material structural characteristics (Fig. 2b). The introduced "electrothermal reduction" mechanism can be divided into three main steps: deoxygenation, formation of structural defects, and sp^2 restoration. Chemically reduced-graphene oxide fibers treated with JH achieved a high electrical conductivity of 1020 S cm^{-1} (Fig. 2c), comparable to bulk graphite ($\sim 10^3$ S cm^{-1}), and are compatible with continuous fiber spinning processes. The advantages and limitations of FJH compared to other repair methods are listed in Table 2.

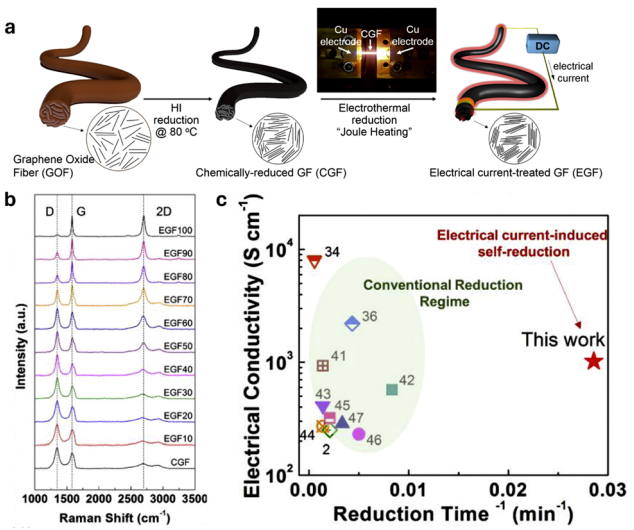

Fig. 2 (a) Experimental procedure for electrothermal reduction of GOF and photoimage of radiating CGF upon electrothermal reduction (Joule heating). (b) Raman spectra of CGF and EGF samples treated at varying levels of maximum input currents (λ_{ex} = 532 nm). (c) Comparative analysis of different reduction methods for graphene fibers in terms of reduction time and electrical conductivity. Reproduced with permission from ref. 57. Copyright 2018 Elsevier.

2.3. Metastable 2D materials

The application of FJH in the conversion of 1T phase materials is highly significant.[61] In addition to the differences in chemical compositions and phase structures, the atomic arrangement within materials significantly influences their chemical properties.[62,63] For example, transition metal dichalcogenide materials are commonly recognized for their layered structure, which manifests in distinctive 1T and 2H phases. The 2H phases exhibit semiconductor characteristics, rendering them applicable in sensing and electrical devices, while the 1T phases demonstrate metallic properties, making them well-suited for employment in electrocatalysts and energy storage devices.[64,65] Because of their outstanding physical and electrochemical characteristics, molybdenum disulfide (MoS_2) and tungsten disulfide (WS_2) have attracted substantial attention in the field of energy conversion and storage.[66,67] However, the synthesis conditions for 1T MoS_2 are challenging, with difficulties in achieving high purity of the 1T phase.[65]

Table 2 Advantages and limitations of different methods for repairing defects in graphene oxide (GO)

Method	Advantages	Limitations	Ref.
FJH	1. Can achieve high temperatures (>2000 °C) instantly, effectively repairing defects in GO. 2. Directional electric field control can influence GO's texture and transport properties. 3. Environmentally friendly and energy-efficient, suitable for continuous fiber spinning processes.	1. Requires precise control of input current, otherwise it may lead to structural and performance non-uniformity.	57
Chemical reduction method	1. Simple operation, no need for high-temperature reactions.	1. Limited reduction effectiveness, incomplete restoration of the sp^2 network. 2. Requires the use of hazardous strong reducing agents.	58
Microwave heating method	1. Rapid heating and short processing time. 2. Material heats uniformly from inside to outside, improving the restoration of GO.	1. Requires precise control of microwave parameters.	59
High-temperature annealing method	1. High degree of GO restoration. 2. Mature technology, simple operation.	1. Requires high temperatures for annealing. 2. Long repair time and high energy consumption.	60

The 1T phase is a metastable form of materials that can easily transition to the more stable 2H phase during synthesis.[68] Traditional synthesis methods such as the hydrothermal method and CVD typically involve gentle temperature changes and prolonged reaction times, which not only fails to maintain the metastable 1T phase but also lead to high energy consumption and low synthesis efficiency. In contrast, FJH offers exceptionally rapid heating and cooling rates, with the capability to control the reaction process within seconds or even milliseconds. This rapid synthesis strategy minimizes the material's exposure to conditions conducive to phase changes, effectively stabilizing it in the 1T phase. And it also reduces energy loss and enhances synthesis efficiency. By precisely controlling the heating process, this technique avoids the phase transition issues common in traditional methods, demonstrating excellent scalability and energy efficiency, and providing feasibility for the rapid, large-scale preparation of metastable materials. Using FJH, Chen *et al.* achieved swift bulk conversions of transition metal dichalcogenides, MoS_2 and WS_2, transitioning from the 2H phase to the 1T phase within a few milliseconds (Fig. 3a).[69] Negative charge doping was reported to be effective in reducing the formation energy of 1T MoS_2 and stabilizing the metastable phase. Tungsten, due to its lower electronegativity, serves as an electron donor when tungsten powder is used as a conductive additive. The conversion rate of flash MoS_2 increased significantly, reaching as high as 76% with the addition of tungsten powder. First-principles density functional theory calculations indicate that the application of FJH, with its high current and substantial energy input, leads to the formation of structural defects, such as S vacancies, and the accumulation of negative charge. This process enables the bulk conversion and stabilization of the metastable 1T phase. Moreover, by adjusting the FJH conditions, such as additives and reaction duration, it is possible to control and achieve different degrees of phase conversion (Fig. 3b and c). Compared to alternative synthesis techniques like ion intercalated methods, ion-assisted chemical vapor deposition, and strong magnetic hydrothermal methods, FJH not only demonstrates rapidity and energy efficiency but also facilitates the bulk conversion of 1T phase materials.

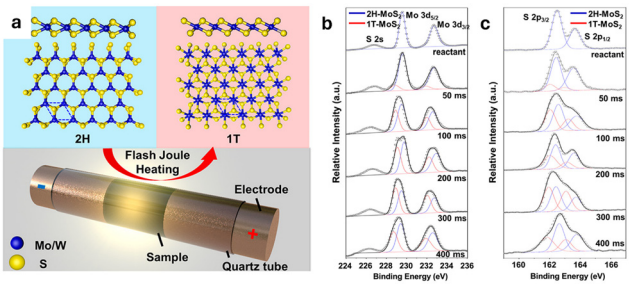

Fig. 3 (a) A schematic representation of the phase conversion by FJH. The inset provides atomic structural representations of the 2H and 1T phases from the side and top view. (b) and (c) High resolution XPS of Mo 3d and S 2p spectra across a range of flash durations from 50 ms to 400 ms. Reproduced with permission from ref. 69. Copyright 2021 American Chemical Society.

As shown in Table 3, compared to other reported materials, flash 1T MoS_2 converted by FJH exhibits relatively low onset overpotential and Tafel slope, indicating its high catalytic activity and excellent reaction kinetics in the hydrogen evolution reaction (HER). As an efficient HER catalyst, flash 1T MoS_2 not only enhances the efficiency of hydrogen production and promotes the utilization of renewable energy but also improves the performance of devices such as fuel cells, thereby advancing the development and application of hydrogen technology. This has a profound impact on the advancement of energy storage technology.

2.4. Boron carbon nitride (BCN)

Boron carbon nitride (BCN) is a multifunctional nanomaterial composed of boron, carbon, and nitrogen elements. Its structure and properties can be easily modulated by slight variations in the arrangement and composition of B, C, and N atoms,

Table 3 Comparison of the HER performance of MoS_2-based electrocatalysts with different synthesis methods

Phase of MoS_2	Method	Onset Overpotential (mV)	Overpotential at 10 mA cm^2 (mV)	Tafel Slope (mV dec^{-1})	Ref.
1T-2H	FJH	142	221	65	69
1T-2H	Chemical exfoliation method	220	550	99	70
1T-2H	Hydrothermal method	175	234	46	71
1T	Liquid exfoliation method	160	312	145	72
2H	Liquid exfoliation method	380	595	125	72
2H	Hydrothermal method	230	330	45	73

allowing it to exhibit various morphological structures such as nanoparticles, nanosheets, and nanotubes.[74] BCN materials possess abundant active sites,[75–77] excellent conductivity,[78] and outstanding chemical stability. Therefore, BCN materials have broad application prospects in energy devices such as lithium batteries, supercapacitors, electrochemical sensors, electrocatalysis, gas separation, and other fields. However, the utilization of BCN materials in energy storage is constrained by their double-layer energy storage mechanism and layered structure.[79] Additionally, the synthesis methods for BCN materials typically entail chemical reactions under high temperature and pressure,[77] which complicates the preparation process and limits its large-scale production and application.

Canonical layered materials typically exhibit thermodynamically stable stacking sequences under standard temperature and pressure.[80] Deviations from these stacking morphologies lead to the formation of disordered lattice structures, introducing unique characteristics of disordered materials.[69,81] However, due to the unfavorable formation energy and spontaneous relaxation toward thermodynamically favorable stacking sequences, the products primarily consist of thermodynamically stable stacking order products,[80,82] making the acquisition of disordered materials challenging.

The FJH method is employed in the synthesis of turbostratic BCN and boron nitride, addressing several shortcomings of traditional methods such as hydrothermal synthesis and CVD. Due to the thermodynamic stability of phases like hexagonal boron nitride (h-BN), products tend to form the most stable layered structures under sustained heat.[82,83] Traditional methods, with their slow cooling rates and prolonged processing times, often lead to well-ordered crystalline structures and it is hard to maintain the desired turbostratic structures. In contrast, FJH offers a cooling process that is 100 to 1000 times faster than hydrothermal and CVD methods. This rapid cooling prevents the material from transitioning to more stable phases, allowing the stabilization of turbostratic structures within milliseconds, significantly enhancing both energy efficiency and synthesis speed. Chen *et al.* synthesized turbostratic boron–carbon–nitride (f-BCN) and carbon-free flash BN (f-BN) with disordered structures using a solid-state FJH system.[84] This method involves heating boron–carbon–nitrogen-containing materials to several thousand degrees Celsius at ultra-fast rates (10^3 to 10^4 K s^{-1}) and then rapidly cooling them at similarly fast rates, achieving the synthesis of f-BCN and f-BN within milliseconds of reaction time (Fig. 4a and b). Experimental results demonstrate that the synthesized f-BCN and f-BN materials exhibit high-quality disordered structures and excellent performance, such as good dispersibility and stability. Compared to commercial h-BN, dispersions formed by f-BCN in 1 wt% Pluronic (F-127) aqueous solution exhibit higher time stability (Fig. 4c and d). When applied in nanocomposite films coated on copper surfaces, f-BCN significantly enhances the corrosion resistance of copper in 0.5 M sulfuric acid (Fig. 4e–h) or 3.5 wt% saline solutions (Fig. 4i–l). Moreover, f-BCN holds potential application prospects in energy storage, catalysis, and materials science fields. The FJH method offers advantages such as rapidity, low cost, and high efficiency, providing a new pathway for the preparation of large quantities of disordered materials. The advantages and limitations of the FJH method compared to other BCN synthesis methods are shown in Table 4.

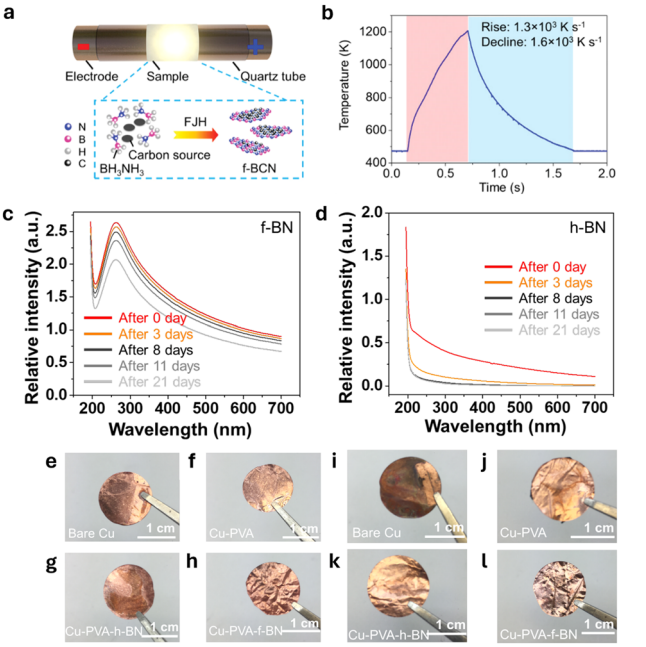

Fig. 4 (a) Schematic diagram for the formation of f-BCN from BH_3NH_3 and carbon through FJH, and (b) the real-time temperature monitoring of the sample during the FJH process. (c) and (d) The UV-vis absorption spectrum of f-BN and commercial h-BN after different sedimentation durations. The optical images of (e) bare Cu, (f) Cu-PVA, (g) Cu-PVA-h-BN and (h) Cu-PVA-f-BN after electrochemical anticorrosion test in 0.5 M H_2SO_4. The optical images of (i) bare Cu, (j) Cu-PVA, (k) Cu-PVA-h-BN and (l) Cu-PVA-f-BN after electrochemical anticorrosion test in 3.5 wt% NaCl (aq). Reproduced with permission from ref. 84. Copyright 2022 Wiley-VCH.

Table 4 Comparison of advantages and limitations of different synthesis methods for BCN

Method	Advantages	Limitations	Ref.
FJH	1. Ultra-fast synthesis speed and high production efficiency. 2. By adjusting the electric current and voltage, the synthesis temperature and time can be precisely controlled, optimizing the structure and performance of BCN. 3. BCN products have excellent dispersibility and stability, better than commercial products. 4. High energy utilization rate, no need for harmful chemicals, environmentally friendly.	1. High equipment safety requirements. 2. Requires precise control of current and heating rate to avoid excessive heat and temperature fluctuations.	84
CVD	1. Easily adjusts the growth conditions to prepare BCN with different compositions and chemical structures.	1. Non-uniform particle composition due to differences in vapor pressure, growth rate, and nucleation process. 2. Precursors like NH_3 are toxic and hazardous. 3. High production cost.	85 and 86
Hydrothermal method	1. High BCN yield. 2. Simple and mature process, relatively low cost.	1. Long reaction time. 2. Requires post-synthesis separation and drying steps. 3. The uniformity of BCN products needs to be improved.	87
Wet-chemical method	1. High purity of BCN products. 2. Good uniformity in size and structure of BCN products.	1. To ensure uniform growth of BCN, optimization of concentration, temperature, pH, and other conditions is required, which can be time-consuming and costly.	88
Pyrolysis	1. Simple operation and short processing time. 2. Good crystallinity of BCN products.	1. Inevitably generates side reactions like oxidation during the process. 2. Low BCN yield.	89 and 90

2.5. Carbon nanotubes (CNTs)

Recently, carbon nanotubes (CNTs) have attracted considerable attention due to their unique structure and excellent properties, including ultra-high surface area and high conductivity comparable to copper.[91] The preformed network of CNT fabrics (CNTFs) serves as ideal scaffolds for the growth of inorganic phases such as ZnO,[92] MnO_2,[93] TiO_2,[94] MoS_2,[95] LFP,[96] *etc.* These electrochemically active materials tightly integrate with the CNTFs, offering not only large surface area, flexibility and strong mechanical strength but also eliminating the need for binders, conductive agents, and even current collectors. This integration shows potential for flexible electrodes, which can improve battery performance. However, traditional methods for synthesizing CNTs, such as CVD and hydrothermal techniques, face several challenges. Typically, these methods are energy-intensive, requiring high temperatures and prolonged processing times, making it difficult to precisely control the properties of the final materials. Particularly, maintaining the desired nanostructure during slow cooling phases poses a significant challenge.[97] Additionally, preserving the structural integrity of CNTs and minimizing adverse reactions such as oxidation are also challenging. In contrast, FJH allows for rapid heating and cooling, significantly reducing total energy consumption and processing time. And this rapid thermal treatment helps effectively stabilize the desired nanostructures, ensuring the structural stability of CNTs. Moreover, compared to materials processed by traditional methods, CNTs prepared *via* FJH exhibit enhanced electrical conductivity and mechanical strength.[25] This improvement is attributed to the rapid crystallization and stabilization of inorganic phases at high temperatures, thereby enhancing the overall functionality of the composites.

Upama *et al.* proposed a novel method for the preparation of CNT fabric and inorganic phase (MoS_2) nanostructure composite materials using JH technology, followed by a study of their structure and properties.[25] In this method, MoS_2 is first electrochemically deposited onto a conductive CNT bundle unidirectional fabric (Fig. 5a). Subsequently, the heat generated by the direct current passing through the CNTs is utilized to crystallize the MoS_2 layer from the inside out (Fig. 5c and d). This enables the rapid preparation of CNTF/MoS_2 composites within minutes, which is significantly more efficient than

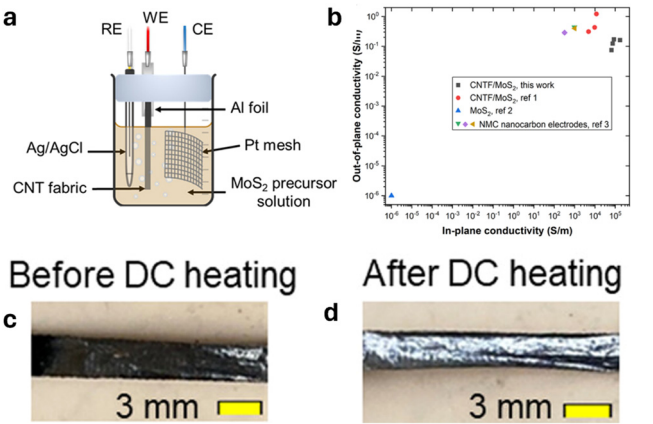

Fig. 5 (a) Depiction of MoS_2 electrodeposition using a three-electrode configuration. (b) Comparison of electrical conductivity achieved in this work with previous research on CNTF/MoS_2, pure MoS_2, and other nanocomposites. (c) and (d) Digital images of a CNTF/MoS_2 (60% MoS_2) sample before and after DC heating. Reproduced with permission from ref. 25. Copyright 2023 American Chemical Society.

Table 5 Comparison of advantages and limitations of different synthesis methods for CNTs

Method	Advantages	Limitations	Ref.
FJH	1. Through adjusting current and voltage, the synthesis temperature and time can be precisely controlled, which is crucial for CNTs uniformity. 2. CNTs produced at high temperatures instantly have high purity, eliminating the need for post-purification. 3. The rapid heating and cooling rates prevent unnecessary oxidation of the CNTs network, achieving enhanced mechanical and electrical properties compared to conventional materials with higher processing temperatures.	1. Requires precise control of current and heating rate to avoid local overheating and temperature fluctuations, which can affect CNTs performance uniformity.	25
CVD	1. Easy reaction control at relatively low working temperatures. 2. High yield and purity of CNTs production. 3. Ability to grow CNTs directly on substrates.	1. The low reaction temperatures result in CNTs with poorer crystallinity. 2. Growth and morphology control of CNTs require catalyst.	98
Laser ablation	1. Capable of producing high-quality, high-purity CNTs in a short time with high yield. 2. By adjusting laser wavelength and energy density, the diameter and length of CNTs can be controlled.	1. Requires high-energy laser, leading to high equipment cost. 2. High reaction temperatures can easily lead to additional defects in CNTs.	99
Flame synthesis method	1. Flame as a reactant provides both chemical and thermal energy, producing various forms of CNTs without the need for external energy supply. 2. By adjusting the ratio of fuel and oxidizer, reaction conditions can be controlled, impacting CNTs morphology and structure.	1. CNTs produced may contain impurities and defects, requiring further processing. 2. Precise control of reaction conditions is relatively difficult.	100
Green synthesis method	1. Uses natural products to replace expensive chemical precursors, reducing production costs. 2. Does not produce toxic residues, reducing the risk of environmental pollution.	1. Reactions require transition metal catalysts. 2. The process is still immature, and the purity and quality of CNTs products need improvement.	101

traditional wet-processed and furnace-heated methods. The JH process is characterized by its rapid and efficient nature, with precise temperature control. Importantly, compared to composites obtained through wet-processed with nanostructured fillers, the CNTF/MoS_2 composites prepared *via* Joule heating exhibit high electrical conductivity ($1.72\ (\pm 0.25) \times 10^5$ S m^{-1}) (Fig. 5b), high tensile modulus (8.82 ± 5.5 GPa), and high longitudinal tensile strength (200 ± 58 MPa SG^{-1}). These properties surpass the specific strength of steel. The electrical conductivity of the CNTF/MoS_2 composite exceeds the threshold of electron transport limitation observed in common battery electrodes, approaching the level achieved by eliminating metallic current collectors. Thus, it shows potential for use in non-metallic battery anodes, offering opportunities for sodium–ion and dual-ion batteries. It can also be extended to other materials and CNT composites, opening up new possibilities for the advancement of high-performance composite materials. The summary of the advantages and limitations of the FJH method compared to other CNT synthesis methods is shown in Table 5.

3. Applications

3.1. Battery electrodes

JH technology is notable for its rapidity, environmental sustainability, cost-effectiveness, and adaptability among various electrode fabrication techniques.[61,102] Electrodes serve as indispensable constituents within energy storage mechanisms, notably in metal–ion batteries encompassing lithium,[103,104] sodium,[105,106] potassium,[107] zinc,[108] and magnesium[109] batteries. Now, considerable advances have been made in electrode research, the application of JH technology has showcased distinct advantages, contributing to advancements in electrode manufacturing processes.[110–112] Here, examples of the application of JH technology in the field of electrodes are summarized (Table 6).

Dong *et al.* effectively reduced graphene oxide (RGO) using the FJH technique, removed numerous oxygen-containing functional groups and prepared defect-rich graphene without complex functional groups within 1 millisecond.[112] The distinctive three-dimensional structural network significantly enhanced the lithium-ion storage capacity and accommodated the expansion of anode during cycling. During the FJH process, a large amount of Joule heat is generated around the conductive paths, and this extremely rapid heating process effectively removes oxygen-containing functional groups. Simultaneously, the loss of some carbon atoms results in a high density of defects on the rGO surface. These defects, which typically have high formation energies and should not appear under thermal equilibrium, are preserved due to the ultrafast annealing rate of FJH, which is a significant advantage over other methods. Moreover, the graphene generated through FJH exhibited a mixed lithium-ion storage mechanism characterized by ''insertion–deposition''. Throughout cycling, the defects within the carbon network synergistically interacted with the locally

Table 6 Summary of Joule heating technique in electrode materials

Type	Materials	Methods (Joule heating behavior)	Initial reversible capacity	Cycling stability (cycle number)	Ref.
LIBs/anode	F-RGO-5	5@200 V × 1 within 1 ms	1480 mA h g^{-1} at 1 A g^{-1}	2450 mA h g^{-1} at 1 A g^{-1} (1000), 1007 mA h g^{-1} at 5 A g^{-1} (5000)	112
Zn micro-battery (ZMB)/cathode	NiCo layered hydroxides (LDH)@CC	∼ 300 W for 13 s	211.2 mA h g^{-1} at 1 A g^{-1}	87.9 mA h g^{-1} at 15 A g^{-1} (5000)	113
LIBs/cathode	$LiMn_2O_4$	∼660 °C for ∼9 s, ∼970 °C for ∼8 s	116.9 mA h g^{-1} at 0.1C	82.5% at 1C (100)	114
	$LiCoO_2$	∼590 °C for ∼29 s, ∼860 °C for ∼16 s	139.5 mA h g^{-1} at 0.1C	84.6% at 1C (300)	
	$LiFePO_4$	∼800 °C for 22 s	142.1 mA h g^{-1} at 0.1C	85.8% at 1C (200)	
	Li-rich layered oxide/NiO	∼650 °C for ∼9 s, ∼700 °C for ∼14 s	87.2 mA h g^{-1} at 5C	—	
Li–O_2 batteries	Carbon nanofibers (CNF)/Pt–Pd–Au–Ru quaternary nanoparticles	A current pulse was applied for 200 ms	9130 mA h g^{-1} at 0.1 A g^{-1}	1000 mA h g^{-1} at 0.5 A g^{-1} (20)	115
SMBs/anode	Na@J1600	40 V, 140 A within seconds	117 mA h g^{-1} at 1C	104 mA h g^{-1} at 1C (300)	116
LIBs/anode	NMS-4-925-1s	190 W with a ramp dwell of 3 s followed by annealing dwells of 1 s	168 mA h g^{-1} at 0.05 A g^{-1}	53 mA h g^{-1} at 0.05 A g^{-1} (100)	111
SIBs/anode	FA3	150 V within 0.1 s for 3 times	209 mA h g^{-1} at 0.05 A g^{-1}	209 mA h g^{-1} at 0.2 A g^{-1} (500)	117
LIBs/anode	CC/CNTs@Ag-Li	60 V, 20 A within 50 ms	155.9 mA h g^{-1} at 0.1C	91.4% at 1C (80)	118
SIBs/anode	GC-2050	140 W, 2050 °C	210 mA h g^{-1} at 0.1 A g^{-1}	200 mA h g^{-1} at 0.05 A g^{-1} (800)	119
LIBs/cathode	LS-LMO	∼670 °C for ∼9 s, ∼740 °C for ∼9 s	109 mA h g^{-1} at 0.1C	83% at 5C (800)	7
LIBs/anode	SnO_2 nanoparticles on CNFs	1 A for 1 s	910 mA h g^{-1} at 0.1C	About 500 mA h g^{-1} at 0.1C (100)	120
LIBs/anode	FHC	300 V for 5 s	321.3 mA h g^{-1} at 0.1C	166.1 mA h g^{-1} at 2C (100)	121
PIBs/anode			262.2 mA h g^{-1} at 0.1C	73.88 mA h g^{-1} at 2C (100)	
LIBs/anode	Us-Si/C	2.1 V 1500 °C for 60 s	2045 mA h g^{-1} at 0.5 A g^{-1}	920 mA h g^{-1} at 2 A g^{-1} (1000), 1.55 mA h cm^{-2} at 3.66 mg cm^{-2} (200)	122
LIBs/anode	Defect-rich cracked flash graphene (CFG)	110 V, 0.1 A for 100–200 ms	551 mA h g^{-1} at 0.05 A g^{-1}	340 mA h g^{-1} (99%) at 1 A g^{-1} (500), 249 mA h g^{-1} (90%) at 5 A g^{-1} (600)	123

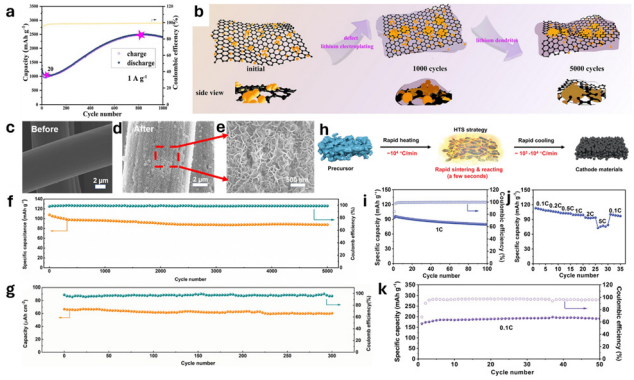

Fig. 6 (a) Cycling performance of F-rGO-5 at a current density of 1 A g^{-1}. (b) A schematic representation illustrating the operating mechanism of F-rGO-5 anode. Reproduced with permission from ref. 112. Copyright 2023 Elsevier B.V. (c)–(e) SEM images of primary CC and NiCo LDH@CC. (f) Cycling performance of NiCo-LDH@CC//Zn alkaline battery. (g) Cycling performance of NC-ZMBs. Reproduced with permission from ref. 113. Copyright 2023 Springer Nature. (h) Schematic description of the HTS synthesis of cathode materials. (i) and (j) Cycling performance at 1C and rate capability of HTS-synthesized $LiMn_2O_4$. (k) Cycling performance of the HTS-synthesized Li-rich layered oxide/NiO heterostructured cathode material at 0.1C. Reproduced with permission from ref. 114. Copyright 2022 Wiley-VCH.

formed "lithium anode" on the surface, leading to remarkable capacity and rate performance, coupled with exceptional cycling stability and high current carrying capacity. After 1000 charge–discharge cycles at 1 A g^{-1}, a reversible capacity of 2450 mA h g^{-1} was attained (Fig. 6a). Furthermore, capacity analysis during 5000 cycles at 5 A g^{-1} revealed the mechanisms for excess lithium storage and its degradation mechanisms in lithium-ion batteries (Fig. 6b). In comparison, defect-rich popcorn-like mesoporous carbon cages derived from lignin, prepared *via* a multistep explosion strategy by thermal decomposition of calcium oxalate, exhibit a reversible capacity of 530.4 mA h g^{-1} at a current density of 1 A g^{-1}.[124] Additionally, defect-rich SnO_2/graphene composites synthesized by microwave-assisted hydrothermal methods show a reversible lithium storage capacity of 653 mA h g^{-1} at a current density of 0.06 A g^{-1} after 100 cycles.[125] The lithium storage capacity of graphene produced by FJH far exceeds these methods. The FJH technology provides novel insights into the design of defect engineering-based high-capacity electrodes and delves into the changes of thin-layer electrodes during cycling, offering significant understanding of the lithium storage mechanism of defective graphene.

Li *et al.* proposed a simple, ultra-fast, and general synthesis method based on Joule heating, using the high reaction kinetics induced by the instantaneous high temperature to synthesize 2D transition metal hydroxides (TM-LDHs) *in situ* on treated conductive carbon cloth (CC) (Fig. 6c–e).[113] This method involves immersing pre-treated carbon cloth in a transition metal salt solution and applying a high current to the carbon cloth, which rapidly generates abundant Joule heat, promoting the hydrolysis of metal salts and quickly forming transition metal hydroxides on the carbon cloth. Traditional synthesis methods, such as hydrothermal synthesis[126] and co-precipitation,[127] require long reaction times, and the products tend to agglomerate, necessitating subsequent tedious processing to uniformly deposit the target material on the conductive substrate. While electrochemical deposition synthesis[128] is also a time-saving method, it inevitably leads to concentration polarization, resulting in uneven deposition and poor crystallinity of the target phase. In contrast, the Joule heating process can synthesize a series of well-structured TM-LDHs within just 13 seconds, achieving a synthesis rate of up to 0.46 cm^2 s^{-1}, surpassing the efficiency of traditional methods. Density functional theory calculations confirmed that the Joule heat generated around the carbon cloth in the FJH method is much higher than the nucleation energy barrier of the metal layered hydroxide phase. And NiCo LDH@CC is presented as an example, demonstrating its outstanding performance as a cathode material for rechargeable aqueous alkaline zinc (micro-)batteries. NiCo LDH@CC exhibits a high specific capacitance (211.2 mA h g^{-1}), high energy density (301.7 W h kg^{-1}), and excellent cycling stability (maintaining 81.4% capacity after 5000 cycles at 15 A g^{-1}) (Fig. 6f). Furthermore, the in-plane flexible quasi-solid-state zinc ion micro-battery assembled with NiCo LDH@CC as the cathode material shows promising capacity (92 μA h cm^{-2}), high energy density (301.7 W h kg^{-1}), and stable cycling performance (maintaining 91.2% capacity after 300 cycles at 3 mA cm^{-2}) (Fig. 6g). This ultra-fast, low-cost synthesis method offers a novel avenue for fabricating metal-based layered hydroxides and presents promising prospects for future growth and development.

Zhu *et al.* presented a high-temperature shock (HTS) strategy for the rapid synthesis of cathode materials using Joule heating[114] Traditional cathode synthesis methods require prolonged annealing at high temperatures, whereas the HTS process offers unique advantages over conventional methods. The HTS process enables a one-step reaction within seconds, directly converting precursors into final products without the need for complex multi-step reaction processes. This approach significantly simplifies the synthesis process and reduces energy consumption compared to traditional methods. The HTS process is characterized by an ultra-high heating rate (approximately 10^4 °C min^{-1}), elevated calcination temperature, and rapid cooling rate (approximately 10^3 to 10^4 °C min^{-1}) (Fig. 6h), leading to non-equilibrium reactions that enhance rapid reaction kinetics while significantly reducing energy consumption and synthesis time. A variety of common cathode materials, including $LiMn_2O_4$, $LiCoO_2$, $LiFePO_4$, and Li-rich layered oxide/NiO heterostructured material have been effectively synthesized. Due to the ultra-high heating and cooling rates and the very short calcination process, these materials exhibit high-purity phases, oxygen vacancies, and ultrafine particle sizes that promote improved electrochemical performance. Among these, $LiMn_2O_4$ synthesized *via* the HTS technique demonstrates superior electrochemical performance compared to conventionally synthesized pure $LiMn_2O_4$ (Fig. 6i and j). The initial discharge capacity of $LiMn_2O_4$ was 116.9 mA h g^{-1}. At a high charge–discharge rate of 5C, the HTS-synthesized $LiMn_2O_4$ maintained a capacity of

78.9 mA h g^{-1}, outperforming other synthesis methods such as solid-state combustion synthesis[129] (73 mA h g^{-1}), colloidal synthesis method[130] (50 mA h g^{-1}), and solid-state synthesis method combined with defect engineering approach[131] (65 mA h g^{-1}). Both $LiCoO_2$ and $LiFePO_4$ demonstrate outstanding cycling stability and remarkable rate capability. Additionally, the Li-rich layered oxide/NiO heterostructured material, synthesized through the HTS technique, exhibits slightly lower discharge capacity than reported Li-rich cathode materials in the literature. However, it showcases excellent rate capability and good cycling stability, with no significant capacity decay observed after 50 cycles (Fig. 6k). The HTS process enables the rapid synthesis of high-performance cathode materials, accelerating the progress of lithium-ion batteries.

3.2. Supercapacitors

The carbon-based material is ideal for supercapacitors and is also an ideal candidate material for Joule heating, which makes Joule heating technology hold tremendous potential for application in supercapacitors. Supercapacitors are high-performance energy storage devices with high power density, superior safety, and long cycle life.[132–134] They can be applied to both low-power electronic products and high-power military equipment.[135] Thus, carbon materials stand as the predominant and pivotal electrode active materials within supercapacitors, and the Joule thermal technology has garnered significant research attention.[136,137] Table 7 summarizes the application of Joule heating in supercapacitor materials.

Zhang *et al.* employed a Joule heating-based high-temperature shock (HTS) technique to synthesize ultrafine structure-activated porous carbon (UAPC) within 10 seconds, without the need for prolonged high temperatures and complex preparation processes.[26] The structural characteristics produced by Joule heating include dense porosity, a stable interconnected framework, and a high degree of disorder. Unlike traditional methods that may lead to the loss of N and O elements during high-temperature treatment, Joule heating, through rapid heating and cooling processes, effectively retains and enriches these functional groups. This significantly enhances the electrode's specific surface area and pseudo capacitance, rendering it a high-energy-density electrode with broad application potential for supercapacitors. The specific surface area of UAPC produced by Joule heating is significantly higher (1384.99 m^2 g^{-1}) compared to APC produced by traditional methods (1048.66 m^2 g^{-1}). In the $EMIMBF_4$ ionic liquid, the supercapacitor based on UAPC exhibited an energy density of up to 129 W h kg^{-1}, far surpassing current advanced and commercial supercapacitors (Fig. 7a) such as the N/O co-doped porous carbon materials prepared by one-step pyrolysis of EDTA and K_2CO_3[151] (17.01 W h kg^{-1}), and the N, S self-doped hollow sphere porous carbon materials prepared by the KOH activation process[152] (58.4 W h kg^{-1}). Additionally, symmetric supercapacitors assembled with UAPC maintain 99% capacitance and 100% Coulombic efficiency even after 4000 cycles at an ultra-high current density of 100 A g^{-1}, demonstrating outstanding cycling stability (Fig. 7b). The superior electrochemical performance of UAPC stems from its rich N, O functional groups and ultrafine structure, which provide high porosity and large specific surface area, thus offering pseudo capacitance and improving surface wettability. This method offers a groundbreaking approach to design high-performance supercapacitors and introduces a novel pathway for the value-added utilization of carbon materials.

Graphene, with its high theoretical surface area, high electrical conductivity, stable chemical properties and excellent mechanical properties, is a promising supercapacitor material.[153–155] Zhu *et al.* developed a novel synthesis method for a material named flash nitrogen-doped graphene (FNG), employing a one-pot, solvent-free, catalyst-free technique known as Flash Joule Heating (FJH).[139] Within a very short time (less than 1 s), the amorphous carbon black and urea precursor were rapidly converted into high-quality FNG through short electrical pulses with bright blackbody radiation flashes. This method generates ultra-high temperatures (>3000 K) with extremely rapid heating and cooling rates, converting samples into FNG in a very short reaction time. The high efficiency of this process significantly surpasses other traditional methods that require long reaction times. The FNG prepared by the FJH method exhibits a high degree of graphitization, turbostratic structure, and minimal structural defects, showcasing excellent electrochemical performance (Fig. 7c). It demonstrates a large surface-area-normalized capacitance of 152.8 μF cm^{-2} at 1 A g^{-1} and maintains capacitance retention of 86.1% even at an extremely high current density of 128 A g^{-1} (Fig. 7d). This performance exceeds that of other synthesis methods, such as N-doped graphene synthesized by thermal annealing[156] (65.1 μF cm^{-2} at 0.6 A g^{-1}), N-doped graphene synthesized by arc discharge[157] (63 μF cm^{-2} at 0.6 A g^{-1}), and two-dimensional nitrogen-doped mesoporous carbon materials synthesized by multistep molecular self-assembly[158] (90.6 μF cm^{-2} at 0.2 A g^{-1}). Furthermore, constructed symmetric quasi-solid-state supercapacitors with the FNG electrode display remarkable energy density (16.9 W h kg^{-1}) and maximum power density (16.0 kW kg^{-1}), maintaining 91.2% capacitance after 10 000 cycles (Fig. 7e). These results showed the substantial potential of FNG within the realm of supercapacitors.

Karim *et al.* utilized millisecond current pulse Joule heating for on-site reduction and activation of perforated graphene, achieving the preparation of multimodal porous frameworks.[140] Traditional thermal activation methods typically require several hours of programmed heating, while chemical etching methods, although feasible at lower temperatures, necessitate hazardous chemical reagents and involve complex purification and post-treatment processes. Compared to traditional thermal activation and chemical etching methods, the current pulse Joule heating method significantly shortens the processing time to just a few milliseconds and is non-toxic and environmentally friendly. Specifically, after a single current pulse lasting 50 ms, dense graphene oxide films on carbon cloth were transformed into non-restacked macroporous graphene frameworks (JG@CC). Controlled perforation of graphene (AJG@CC) was then achieved through continuous 100

Table 7 Summary of Joule heating technique in supercapacitors

Materials	Methods (Joule heating behavior)	Electrolyte	Voltage window	Specific capacitance	Energy density	Power density	Cycling stability	Ref.
Ultrafine structure-activated porous carbon (UAPC)	900 °C within 10 s	$EMIMBF_4$	0–4 V	602 F g^{-1} at 1 A g^{-1}, 400 F g^{-1} at 20 A g^{-1} (6 M KOH, three-electrode)	129 W h kg^{-1}	1667 W kg^{-1}	99% capacitance after 4000 cycles at 100 A g^{-1}, Coulombic efficiency 100%	138
Flash nitrogen-doped graphene (FNG)	180 V, >3000 K within 200 ms	PVA/KOH	0–1 V	175.1 F g^{-1} at 1 A g^{-1}, 150.7 F g^{-1} at 128 A g^{-1} (6 M KOH, three-electrode)	16.9 W h kg^{-1}	16.0 kW kg^{-1}	91.2% capacitance after 10 000 cycles	139
Activated rGO sheets over carbon cloth (AJG@CC)	20 numbers of 30 V pulses, 100 ms each, time gaps 1 s	PVA/H_2SO_4	0–1.6 V	380.2 mF cm^{-2} at 5 mV s^{-1} (1 M H_2SO_4, two-electrode)	107.77 μW h cm^{-2}	485 μW cm^{-2}	94% capacitance after 10 000 cycles at 50 mA cm^{-2}, coulombic efficiency 100%, 90% capacity retention rate after more than 5000 repeated bending and folding cycles.	140
RuO_2-decorated nitrogen- and sulfur-doped graphene fibers (NS-GF@RuO_2)	A direct current of 35 mA, 0.5 s	PVA/H_2SO_4	0–1 V	68.88 F g^{-1} at 0.2 A g^{-1} (PVA/H_2SO_4, three-electrode)	0.833–2.93 W h kg^{-1}	36.72–1428.57 W kg^{-1}	96.67% capacitance after 20 000 cycles at 5 A g^{-1}, Coulombic efficiency 100%	141
CNT/1,3,5-tris(2′-bromophenyl)benzene (2TBB) fibers	140 V	PVA/H_3PO_4	0–0.8 V	50 F cm^{-3} at 0.05 A cm^{-3}	4.5 mW h cm^{-3}	1.3 W cm^{-3}	—	142
Nitrogen-doped carbon nanotubes (N-CNTs)	80 V, 1300 K within 1 s	1 M KOH	−0.2 to 0.8 V	101.7 mF cm^{-2} at 5 mV s^{-1} (1 M KOH, three-electrode)	1.03 μW h cm^{-2}	—	83% capacitance after 10 000 cycles at 2 mA cm^{-2}	143
High-temperature shock activated porous carbons (HTS-APC)	1100 K within 10 s	$EMIMBF_4$	0–3.5 V	152.87 F g^{-1} at 1 A g^{-1} (6 M KOH, three-electrode)	25 W h kg^{-1}	582 W kg^{-1}	98.64% capacitance after 10 000 cycles at 20 A g^{-1}, Coulombic efficiency 100%	8
Joule-heated laser-induced graphene paper (J-LIGP)	138 V, 500 °C for 60 min	PVA/H_3PO_4	0–1 V	13.71 mF cm^{-2} at 10 mV s^{-1}	—	—	95.94% capacitance after 10 000 cycles at 1 mA cm^{-2}	144
Joule-heating activated CF (JACF)	7 V for 10 min	PVA/H_3PO_4	0–1 V	162 F g^{-1} at 0.5 A g^{-1} (1 M H_2SO_4, three-electrode)	—	—	97% capacitance after 5000 cycles at 10 A g^{-1}	145
PP-5.0-12.5	5 V for 12.5 min	0.5 M Na_2SO_4	0–2 V	190.33 mF cm^{-2} at 0.5 mA cm^{-2} (0.5 M Na_2SO_4, three-electrode)	—	—	97.36% capacitance after 10 000 cycles at 2.0 mA cm^{-2}	146
Electrically treated graphene fibers (EGFs)@NiO	160 mA for 50 s	PVA/KOH	0–1.5 V	110.36 F cm^{-3} at 0.5 A cm^{-3}	34.49 mW h cm^{-3}	374.97 mW cm^{-3}	81.7% capacitance after 7000 cycles at 10 A cm^{-3}, Coulombic efficiency 100%	147
Joule-heating pyrolyzed carbon fiber cloth (CFC-5.0–12.5)	5 V for 12.5 min	0.5 M Na_2SO_4	0–2 V	111.6 mF cm^{-2} at 0.2 mA cm^{-2} (0.5 M Na_2SO_4, three-electrode)	—	—	94% capacitance after 10 000 cycles at 1.0 mA cm^{-2}	148
Amorphous carbon-CNT fibers (aC-CNT)	140 V	PVA/H_3PO_4	0–0.8 V	5.1 F cm^{-3} at 118 mA cm^{-3}	—	—	94% capacitance after 10 000 cycles at 14 mA cm^{-3} when deformed (90° bend)	149
Joule heating-activated carbon fibers (JACF)	Joule heating reduced at 800 °C for 5 min, and evaporated at 1200 °C for 1 min	PVA/H_3PO_4	0–1 V	268 F g^{-1} at 1 A g^{-1} (three-electrode)	12.6 W h kg^{-1}	4275 W kg^{-1}	79.5% capacitance after 5000 cycles at 2 A g^{-1}	150

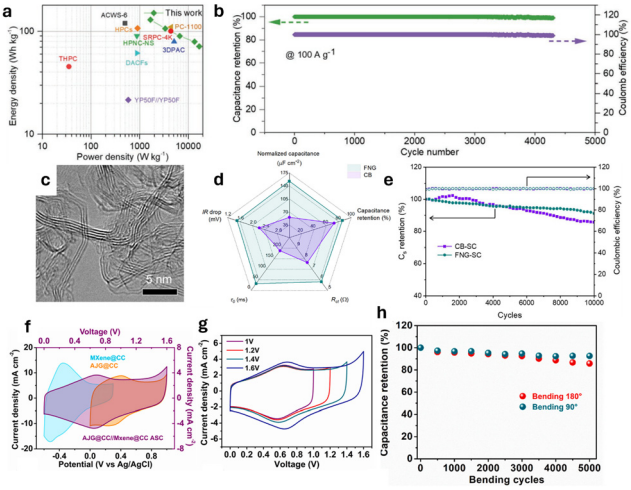

Fig. 7 (a) Ragone plots and the comparison of energy and power densities with some similar reported materials in $EMBMIF_4$ electrolyte. (b) Cycling stability of UAPC//UAPC at 100 A g^{-1}. Reproduced with permission from ref. 26. Copyright 2022 Wiley-VCH. (c) TEM images of flashing graphene (FG). (d) Radar plots of FNG and CB electrodes involving area-normalized capacitance (μF cm^{-2}) at 1 A g^{-1}, capacitance retention (%) at 128 A g^{-1}, R_{CT} (Ω), τ_0 (ms), and IR drop (mV) at 1 A g^{-1}. (e) Capacitance retention and Coulombic efficiency of CB and FNG based quasi-solid-state SCs over 10 000 cycles. Reproduced with permission from ref. 139. Copyright 2022 American Chemical Society. (f) CV curves of MXene@CC, AJG@CC electrodes, and assembled AJG@CC//MXene@CC asymmetric solid-state Supercapacitor (ASC) at 10 mV s^{-1}. (g) CV curves of ASC measured over operating voltage windows from 1 to 1.6 V at 10 mV s^{-1}. (h) Bending stability test for 5000 continuously repeated bending cycles at the angles of 90° and 180°. Reproduced with permission from ref. 140. Copyright 2022 Elsevier.

ms ultra-short current pulses activated by KOH. By employing transient current modulation to tailor the multi-peak porosity and surface functionality of graphene, the fabricated electrodes demonstrated an energy density of 52.8 μW h cm^{-2} and an areal capacitance of up to 380.2 mF cm^{-2} in a symmetric dual-electrode configuration. Compared to similar products without electrochemical activation (238.8 mF cm^{-2}), the performance of AJG@CC is 1.6 times higher. Furthermore, employing AJG@CC as the cathode and titanium carbide nanosheets (MXene) as the anode, a high-performance wearable asymmetric supercapacitor was achieved. It demonstrated a high areal energy density of 107.8 μW h cm^{-2} and an extended potential window of 1.6 V at a power density of 485 μW cm^{-2} (Fig. 7f and g), surpassing symmetric devices with approximately 1 V potential window. Even at an extremely high areal power density of 4404.54 μW cm^{-2}, it maintained a high areal energy density of 83.88 μW h cm^{-2}. Additionally, the wearable device exhibited excellent cycling stability and outstanding operational durability, with a capacity retention rate of 94% after 10 000 cycles and over 90% high-capacity retention rate after more than 5000 repeated bending and folding cycles (Fig. 7h).

3.3. Electrode material recycling

As a novel technology with high efficiency, minimal energy usage, and eco-friendliness, Joule heating holds promise for electrode material recycling. With the rapid updating of electronic devices and the increasing popularity of electric vehicles, the demand for lithium-ion batteries (LIBs) has consistently experienced rapid growth. Because lithium-ion batteries (LIBs) have a restricted lifespan, it is anticipated that a significant number of depleted LIBs will be discarded within 5–10 years.[159] Facilitating the recycling of high-value metals (*e.g.*, Li, Co, Ni, Mn) in electrode materials[160] and the regeneration of spent graphite[161] are conducive to achieving sustainable development and carbon neutrality.[162] Currently, cathodes are recycled through hydrometallurgical and pyrometallurgical processes,[163–165] and anodes such as graphite are burned or landfilled. However, hydrometallurgical processes necessitate the utilization of acids, alkalis, and other chemicals, leading to the production of significant wastewater.[166] Pyrometallurgical methods involve the use of reducing agents, which results in elevated energy consumption and the emission of harmful gases.

Dong *et al.* achieved the efficient recycling of large volumes of spent graphite in a brief period using the modified flash Joule heating (FJH) technique.[161] The high-temperature environment (>3000 K) ensures the efficient elimination of the binder, components of solid electrolyte interphase (SEI), including LiF and Li_2CO_3, and lithium embedded in the graphite layer. The FJH method rapidly elevated the temperature of waste graphite to 3000 K within a very short time, effectively repairing graphite defects and reconstructing its crystal structure, resulting in recovered graphite with electrochemical performance close to that of new graphite. Simultaneously, the electric field directs the pyrolysis byproducts of the conductive agent and the binder, leading to the creation of conductive sheet graphene and curled graphene, which coat the surface of the graphite. This enhances the electrical conductivity of the recycled graphite, surpassing that of new commercial graphite. Another advantage of the FJH method is that it eliminates the need for complex heating steps and strong corrosive solvents, allowing the product to be used directly without additional treatment. The regenerated graphite demonstrates outstanding rate performance and cycling stability, achieving a capacity of 350 mA h g^{-1} at 1C with a capacity retention of 99% after 500 cycles (Fig. 8a), outperforming regenerated graphite produced by other regeneration methods such as the deep eutectic solvent method[167] (288.0 mA h g^{-1} at 1C) and the heat treatment method[168] (230.3 mA h g^{-1} at 1C). This occurs because impurities are removed during the Joule heating phase, enhancing graphitization and interlayer spacing (Fig. 8b and c), thereby rendering the reclaimed graphite more compatible for lithium-ion intercalation and deintercalation.[169] Additionally, the cost of regenerated graphite obtained through the FJH method is only 77 CNY per ton, whereas the current price of commercial battery-grade graphite is about 30 000 CNY per ton. The FJH method achieves the regeneration of waste graphite not only providing significant economic benefits but also realizing the reuse of waste resources, reducing carbon waste and environmental pollution, making it a highly promising green regeneration technology.

Chen *et al.* developed an ultrafast flash recovery technique for regenerating graphite anodes and recovering valuable

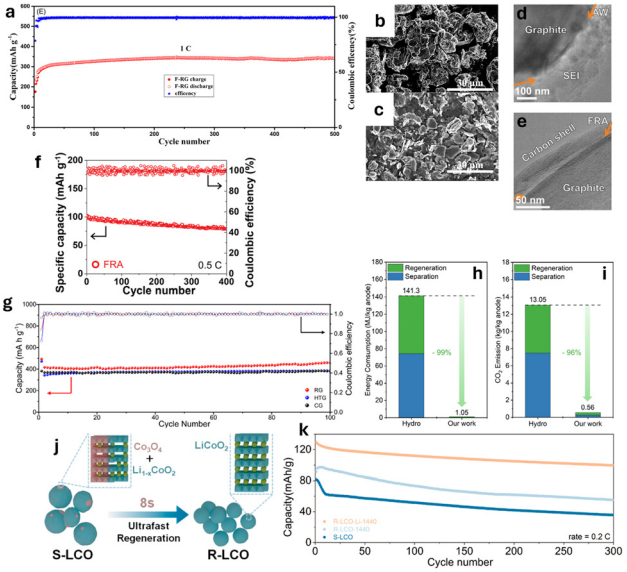

Fig. 8 (a) Cycle performance and Coulombic efficiency at the current density of 1C of F-RG. (b) and (c) SEM images of spent graphite and F-RG. Reproduced with permission from ref. 161. Copyright 2022 The Hong Kong Polytechnic University and John Wiley & Sons Australia. (d) and (e) AW and FRA microparticles. The yellow arrows delineate the boundaries of graphite particles. AW: anode waste. FRA: flash-recycled anode. (f) Cycling performance of FRA with a $LiFePO_4$ cathode at 0.5C. Reproduced with permission from ref. 170. Copyright 2022 Wiley-VCH. (g) Cycling performance of RG, HTG, and CG at a current density of 0.2 A g^{-1}. RG: regenerated graphite. HTG: spent graphite with the same heating treatment but without the addition of Sn. CG: commercial graphite. (h) The total energy consumption, and (i) the CO_2 emission. Reproduced with permission from ref. 171. Copyright 2023 Wenzhou University and John Wiley & Sons Australia. (j) Schematic of the repair process of S-LCO. S-LCO: spent $LiCoO_2$. (k) Cycling performance of S-LCO, R-LCO-Li-1440, and R-LCO-Li-1440 at 0.2C. Reproduced with permission from ref. 172. Copyright 2023 American Chemical Society.

battery metal resources.[170] The resistive SEI was decomposed using the flash Joule heating technique and a carbon shell was formed around graphite microparticles, preserving the intrinsic 3D layered graphite core structure (Fig. 8d and e). Simultaneously, simple inorganic salts such as LiF and metal oxide nanoparticles such as Li_2O and CoO are generated through the decomposition of the SEI layer and other impurities are retained during the ultrafast treatment process. The metals Li, Co, Ni, and Mn can be readily reclaimed from the flash anode products by subsequent treatment with 0.1 M HCl. In contrast, traditional thermal treatment methods, due to their slow heating and cooling process, often result in metals being ultimately discharged as vapor, leading to metal resource wastage and environmental pollution. The anode after flash treatment demonstrates a restored specific capacity of 351.0 mA h g^{-1} at 0.2C and satisfactory electrochemical stability. With a $LiFePO_4$ cathode coupling, the capacity retention stands at 77.3% after 400 cycles at 0.5C (Fig. 8f). Furthermore, compared to synthetic graphite production methods, FJH significantly reduces recovery costs by approximately 85%, and by 50% compared to traditional high-temperature calcination methods. More importantly, FJH notably reduces greenhouse gas emissions by about 98%, water usage by 92%, and energy consumption by 96% compared to synthetic graphite production. Compared to high-temperature calcination recovery methods, FJH reduces greenhouse gas emissions by 51%, water usage by 39%, and energy consumption by 50%. This technology not only offers substantial economic benefits but also significantly reduces the environmental impact of graphite production and regeneration, showing great potential for large-scale production.

Cheng *et al.* developed a rapid, energy-efficient, and targeted defect remediation method to regenerate and upgrade spent graphite.[171] With a high capacity and low melting point, Sn was used as a nano-scale repair agent for the targeted repair of graphite. Flash-Joule heating delivers a high temperature of 1600 °C within 50 ms, thermally reducing loaded $SnCl_2$ on spent graphite to molten Sn. Sn droplets preferentially nucleate and cool on defects of spent graphite due to a stronger binding energies between Sn and defects compared to Sn and graphite. This process achieves the dispersion of Sn and the regeneration of graphite. The ultra-fast heating and cooling rates of FJH enable an effect that other regeneration methods cannot achieve. The regenerated graphite demonstrates a substantially higher capacity than commercial graphite and other regenerated graphite produced by other methods such as high-temperature treatment and acid leaching, reaching 458.9 mA h g^{-1} (Fig. 8g) after 100 cycles at 0.2 A g^{-1}. This is attributed to the precise dispersion of Sn particles and the retained lithium storage activity following graphite regeneration, showcasing excellent cycling stability. According to EverBatt's analysis, this approach proves to be not only environmentally sustainable (Fig. 8h) but also economically advantageous (Fig. 8i) compared to traditional hydrometallurgical recycling methods, underscoring its significant economic promise.

Yin *et al.* introduced a highly efficient, one-step, nondestructive approach to regenerate spent $LiCoO_2$ cathodes, taking only 8 seconds at the optimal reaction temperature of 1440 K through rapid Joule heating.[172] This approach achieves both the relithiation of the cathode material and the restoration of the crystal structure simultaneously (Fig. 8j). Systematic characterization techniques indicate that the instantaneous high temperature generated by FJH can quickly restore the crystal structure of the cathode material while avoiding lithium loss, which is often caused by prolonged high-temperature treatments. The phase structure of the waste $LiCoO_2$ is completely restored to its original layered structure. The optimized repaired $LiCoO_2$ regains an initial discharge capacity of 133.0 mA h g^{-1} at 0.1C, demonstrating excellent cycling performance for over 300 cycles (Fig. 8k). Moreover, the repaired $LiCoO_2$ exhibits superior rate capacity, surpassing the performance of the furnace-repaired sample and comparable to that of the pristine materials. Traditional high-temperature annealing is a common regeneration process for $LiCoO_2$. In contrast, this method requires prolonged high-temperature treatment, which is time-consuming, energy-intensive, and unable to

control lithium volatilization. The discharge capacity of $LiCoO_2$ cathode material regenerated using this traditional method is 111.4 mA h g^{-1}, lower than the performance achieved by FJH.

3.4. Solid state electrolyte

Utilizing Joule heating for the ultrafast sintering of solid-state electrolytes holds promising potential. As the demand for lithium-ion batteries increases across diverse applications, conventional designs employing liquid or gel electrolytes are proving insufficient to meet this growing demand.[173–176] All-solid-state batteries have received significant attention due to their high safety, wide voltage window, high energy density, and long cycle life.[177–180] Solid-state electrolyte (SSE) is the most critical component of solid-state batteries, determining the development of all-solid-state batteries, including NASICON-type,[181–183] LISICON-type,[184,185] perovskite-type,[186,187] garnet-type,[188,189] sulfide-based superionic conductors.[190,191] Some of the applications of solid electrolyte materials using Joule heating are listed in Table 8.

Wang *et al.* utilized carbon heaters-based Joule heating to rapidly sinter thin, porous 3D ceramic SSE scaffolds at high temperatures (1273 K) within seconds (Fig. 9a).[192] This approach achieves precise control over the sintering process by controlling the sintering temperature and duration, thereby restricting overall densification, and minimizing the loss of volatile elements, which applies to various substrates, including Al_2O_3 sheets, titanium, stainless steel, and carbon paper, demonstrating its versatility in different applications. Unlike traditional sintering methods that require several hours, the Joule heating method can quickly reach high temperatures, completing the entire sintering process within seconds. This limits grain growth and coarsening while promoting neck growth between grains without full densification, preserving the porous structure crucial for lithium-ion transport. This enables the achievement of pure crystal phases and the intended porous structure. To verify the concept, LiTFSI and polyethylene oxide (PEO) were infiltrated into LLZTO, LLZTO serving as a 3D porous SSE scaffold model material. This composite SSE was then tested for its ion conductivity using electrochemical impedance spectroscopy (Fig. 9b). The results revealed a high ion conductivity of 1.9×10^{-4} S cm^{-1} at room temperature for the composite SSE, demonstrating the excellent performance of the 3D porous SSE scaffold sintered using this method. Traditional sintering methods usually demand several hours,[202] whereas Joule heating sintering merely takes a few seconds, making it simpler, more efficient, and significantly cutting down time costs.

Wang *et al.* developed an ultrafast high-temperature sintering (UHS) technique employing Joule heating for ceramics.[16] Ceramics provide outstanding mechanical, thermal, and chemical stability, making them ideal candidates for solid-state electrolyte materials. However, traditional ceramic sintering techniques usually entail lengthy processes at high temperatures, leading to considerable time and energy consumption, along with substantial loss of volatile elements.[203] In an inert atmosphere, the UHS technique rapidly heats carbon heating elements to temperatures as high as 3000 °C, facilitating the synthesis and sintering of ceramic materials within seconds (Fig. 9c–e). Due to the short sintering time, the UHS technique effectively prevents the evaporation of volatile elements and undesirable interfacial diffusion in multi-layer structures, significantly reducing lithium loss. For instance, in LLZTO samples, lithium loss is below 4%, whereas traditional furnace-sintered samples experience lithium loss as high as 99%. The technique ensures uniform temperature distribution, high heating and cooling rates, bypassing the low-temperature region, reducing particle coarsening, and maintaining high sintering capillary driving force. The LLZTO sintered with UHS technique exhibited relatively small grain sizes of 8.5 ± 2.0 μm (compared to 13.5 ± 5 μm with traditional furnace sintering) and achieved approximately 97% high relative density. Moreover, the short sintering time effectively prevented significant lithium loss due to Li evaporation. The UHS LLZTO samples exhibited an ultra-high ionic conductivity of approximately 1.0 ± 0.1 mS cm^{-1} (Fig. 9f), surpassing that of the majority of garnet-based SSEs. Other LLZTO sintering methods, such as traditional furnace sintering at 1200 °C for 20 minutes, produce LLZTO samples with ionic conductivity of 8.1×10^{-4} S cm^{-1}.[204] Another relatively novel method, CO_2 laser sintering, results in LLZTO films with an ionic conductivity of 0.26 mS cm^{-1},[205] both inferior to the UHS technique based on Joule heating.

Zuo *et al.* introduced an innovative ultrafast high-temperature synthesis (UHS) method for the direct production of NASICON-type solid-state sodium ion conductors $Na_{3.3}Zr_{1.7-}Lu_{0.3}Si_2PO_{12}$ (NZLSP) from blended precursor powders.[181] Utilizing Joule Heating, the method substantially diminishes synthesis duration from multiple hours to just seconds, resulting in the production of pure NASICON phase samples. The UHS technique eliminates the formation of undesirable secondary phases commonly found in traditional methods, thus enhancing the uniformity and purity of the final material. UHS has been demonstrated to be viable for producing the NASICON phase only when specific dopants like Tm, Yb, and Lu are employed. However, conventional dopants such as Mg, Zn, Y, Hf, and La cannot be synthesized using the UHS method. Experimental results suggest that certain dopants, such as Lu, can generate an intermediate phase, facilitating the formation of the NASICON phase. This process lowers the reaction barrier and promotes uniform diffusion of elements. Moreover, NZLSP solid electrolytes produced through UHS exhibit a remarkable ionic conductivity of 7.7×10^{-4} S cm^{-1} at room temperature, approximately three times greater than that of the undoped $Na_3Zr_2Si_2PO_{12}$ (NZSP) synthesized using conventional methods (Fig. 9g), while displaying negligible electronic conductivity. Assembled symmetric sodium cells exhibit exceptional stability, cycling for over 4800 hours without dendrite penetration (Fig. 9h). Additionally, NASICON-based solid-state sodium batteries exhibit enhanced discharge specific capacity and Coulombic efficiency after Lu doping, showcasing improved performance. In contrast, the 3D-NZLSP composite solid-state electrolyte (3D-NZLSP-CSE) prepared by *in situ* polymerization

Table 8 Application of Joule heating in the synthesis of solid electrolytes

Electrolyte	Materials	Methods (Joule heating behavior)	Ionic conductivity (S cm^{-1})	Electrochemical stability	Ref.
Garnet	P-LLZTO/PEO	1273 K within 10 s	1.9×10^{-4} (RT)	—	192
Garnet	Ta-doped $Li_{6.5}La_3Zr_{1.5}Ta_{0.5}O_{12}$ (LLZTO)	1500 °C within 10 s	$1.0 \pm 0.1 \times 10^{-3}$ (RT)	The Li-LLZTO-Li symmetric cell with a thick (>100 μm) Li metal coating demonstrates a critical current density as high as 3.2 mA cm^{-2}. Cycle for >400 hours at a current density of 0.2 mA cm^{-2}.	16
NASICON	$Na_{3.3}Zr_{1.7}Lu_{0.3}Si_2PO_{12}$ (NZLSP)	1880 K within 8 s	7.7×10^{-4} (RT)	The Na|NZLSP|Na symmetric cells demonstrate a critical current density of up to 1.4 mA cm^{-2}. Cycling over 4800 h at 0.1 mA cm^{-2} without dendrite penetration.	181
Garnet	Ta-doped $Li_7La_3Zr_2O_{12}$ (LLZTO)	28 V, 25 A, 1500 K within 30 s	6.4×10^{-4} (298 K)	The Li|LLZTO membrane|Li symmetric cell demonstrated stable operation up to 300 h at a current density of 0.2 mA cm^{-2} without shorting or any abnormal polarizations. Stable in the cycling performance when current density increased from 0.1 mA cm^{-2} to 0.65 mA cm^{-2}.	193
Perovskite	$Li_{0.348}La_{0.55}TiO_3$ (LLTO)	28 V, 25 A, 1500 K within 30 s	1.4×10^{-3} (298 K)	—	
Garnet	$Li_{6.5}Nd_3Zr_{1.5}Ta_{0.5}O_{12}$ (LNZTO)	1773 K within 10 s	2.3×10^{-4} (30 °C)	The Li/LNZTO/Li cell showed smoother profiles with a critical cycle current density of 1.4 mA cm^{-2}. The Li/LNZTO/Li showed a more stable plating/stripping characteristic with an overpotential of ≈40 mV. After ≈90 h, the Li/LNZTO/Li cell showed no obvious deterioration in terms of overpotentials.	194
Garnet	$Li_{6.5}Sm_3Zr_{1.5}Ta_{0.5}O_{12}$ (LSZTO)	1773 K within 10 s	8.3×10^{-5} (30 °C)	The Li/LSZTO/Li demonstrated a critical cycle current density of 1 mA cm^{-2}. The Li/LSZTO/Li cell showed no obvious deterioration in terms of overpotentials within ≈ 50 h.	
Garnet	$Li_{6.5}(Sm_{0.5}La_{0.5})_3Zr_{1.5}Ta_{0.5}O_{12}$ (L-LSZTO), with Ehull <40 meV per atom	1773 K within 10 s	1.75×10^{-4} (30 °C)	The Li/L-LSZTO/Li demonstrated a critical cycle current density of 1.2 mA cm^{-2}. The symmetrical cell employing L-LSZTO cycled for an additional 30 h using a current density of 0.4 mA cm^{-2} compared to that of LSZTO.	
Garnet	$Li_{6.25}Al_{0.25}La_3Zr_2O_{12}$	60 V cm^{-1}, 200 mA mm^{-2}, 10 s	3.1×10^{-4} (25 °C)	—	195
Garnet	$Li_{6.25}Al_{0.25}La_3Zr_2O_{12}$	50 V cm^{-1}, 150 mA mm^{-2}, 30 s	1.8×10^{-4} (RT)	—	196
Garnet	Al-doped $Li_{6.75}La_3Zr_2O_{12}$	1250 °C within 0.4 s	3.2×10^{-4} (RT)	The critical cycling current density in symmetric cells increased from 100 μA cm^{-2} to 500 μA cm^{-2}.	197
NASICON	$Na_3Zr_2Si_2PO_{12}$ (NZSPO)	10 A, 6 s, 20 A, 60 s, 10 A, 10 s	2.62×10^{-4} (25 °C)	Na|US-NZSPO|Na symmetric cell delivers a cycling time over 270 h with a steady voltage overpotential at a current density of 0.5 mA cm^{-2}. A Coulombic efficiency of 99.9% and capacity retention of 89% are achieved at 0.2C in $Na_3V_2(PO_4)_3$ (NVP)|US-NZSPO|Na solid cells after 800 cycles with the areal NVP loading of 4.5 mg cm^{-2}.	198
Garnet	$Li_7La_3Zr_2O_{12}$ (LLZO)	1200 °C within 90 s	1.4×10^{-4} (RT)	Li/LLZO/Li symmetric cell exhibited a critical current density of up to 1.7 mA cm^{-2} and cycling stability of over 160 cycles at a current density of 0.4 mA cm^{-2}.	199
Garnet	Li_3N/Ta-doped $Li_7La_3Zr_2O_{12}$ (LLZTO)	1600 K within 20 s	1.09×10^{-3} (298 K)	The Li|Li_3N/LLZTO|Li cell exhibited a critical current density (CCD) of 2.3 mA cm^{-2}. The Li|Li^3N/LLZTO|Li cell can be cycled for 500 h with a low overpotential of 8 mV at a current density of 0.2 mA cm^{-2} and for 160 h at a current density of 0.5 mA cm^{-2}.	200
NASICON	$Li_{1.5}Al_{0.5}Ge_{1.5}(PO_4)_3$ (LAGP)	~19 A, 180 s, ~750 °C	1.15×10^{-4} (RT)	—	201

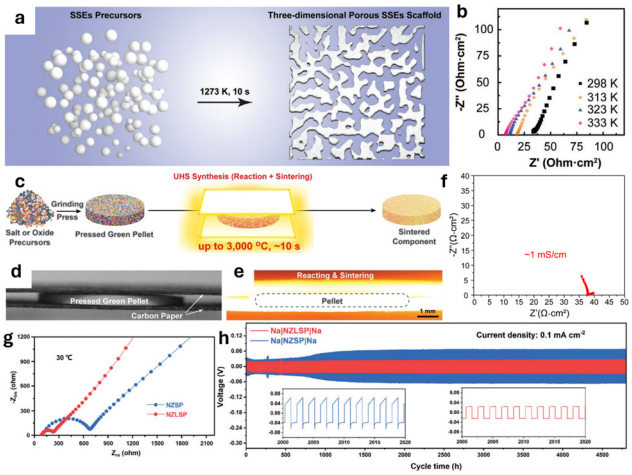

Fig. 9 (a) Transformation of precursor powders to 3D porous SSE scaffolds at 1273 K for 10 s by ultrafast sintering technique. (b) Nyquist plots of the stainless-steel/composite electrolyte/stainless-steel symmetrical cell with temperature ranging from 298 to 333 K. Reproduced with permission from ref. 192. Copyright 2021 Wiley-VCH. (c) Schematic of the UHS synthesis process. (d) Photographs of the UHS sintering setup at room temperature without applying current, and (e) at ~1500 °C. (f) Typical EIS measurement of the UHS-sintered garnet SSE, made with a sintering temperature of 1500 °C for 10 s. Reproduced with permission from ref. 16. Copyright 2020 The American Association for the Advancement of Science. (g) Room-temperature EIS plots of NZSP and NZLSP SSEs. (h) Prolonged galvanostatic cycling of Na|NASICON|Na symmetric battery with NZSP and NZLSP SSEs at a current density of 0.1 mA cm^{-2}. Reproduced with permission from ref. 181. Copyright 2023 Wiley-VCH.

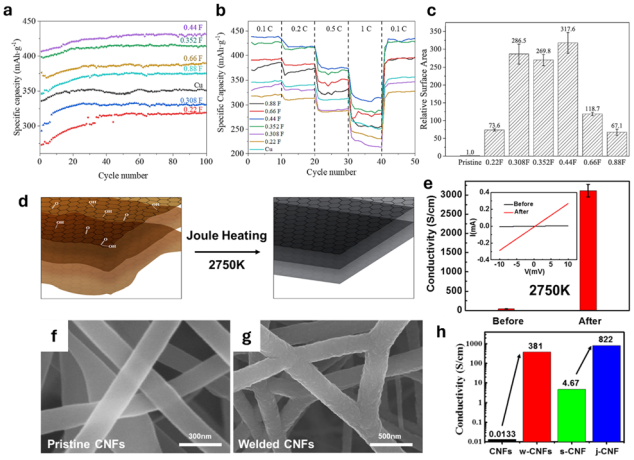

Fig. 10 (a) Cycling performance and (b) rate discharge performance of lithium-ion batteries assembled with Joule-heated samples. (c) The electrochemical active surface area of Joule-heated samples was obtained from different capacitance preparations. Reproduced with permission from ref. 210. Copyright 2023 Elsevier B.V. (d) Joule heating at 2750 K for 1 min in vacuum can effectively reduce the RGO. (e) The conductivity of RGO film before and after the 2750 K reduction by the Joule heating. The inset shows the linear scan of the I–V curve. Reproduced with permission from ref. 216. Copyright 2016 American Chemical Society. (f) and (g) SEM images of the pristine CNF and welded CNF. (h) The conductivity of pristine CNF film (CNFs), welded CNF film (w-CNFs), a single fiber CNF (s-CNF), and a Joule heated single fiber CNF (j-CNF). Reproduced with permission from ref. 217. Copyright 2016 American Chemical Society.

on a 3D ceramic framework requires annealing at 1000 °C for 24 hours, making the process cumbersome and time-consuming compared to the UHS method based on Joule heating. The 3D-NZLSP-CSE, when applied to solid-state sodium batteries, exhibited an ionic conductivity of 4.825 × 10^{-4} S cm^{-1}, which is lower than that of NZLSP synthesized by the UHS method.[206] Utilizing Joule heating, the UHS technique offers an efficient, time-saving, and energy-efficient method for the swift synthesis of NASICON-type solid-state electrolytes. This advancement facilitates the exploration and utilization of intricate functional materials.

3.5. Current collectors

The current collector materials prepared with Joule heating assistance can significantly enhance the performance of lithium-ion batteries (LIBs), which is an essential component of LIBs. Commercial batteries still use traditional current collectors, with aluminum foil for the cathode and copper foil for the anode. To achieve superior performance in the next generation of LIBs, it is crucial to enhance the performance of the current collector.[207] For example, reducing the weight ratio of the current collector, enhancing its electrical conductivity, minimizing contact resistance, and improving corrosion resistance are beneficial for improving the capacity, rate performance, cycling stability, and energy density of LIBs.[208,209]

Lin *et al.* used a transient Joule heating device powered by a capacitor as the heat source for vapor-phase dealloying (VPD), achieving the rapid formation of three-dimensional nano-porous copper in mere seconds.[210] These copper nano-porous materials serve as vital functional components across various fields, particularly in energy storage,[211,212] catalytic reactions,[213] filtration separation,[214] adsorption,[215] *etc.* During the Joule heating process, the high temperature generated by the instantaneous release of large currents can effectively promote the evaporation of zinc from brass, forming a porous copper structure. As the capacitance increases, the dezincification of the VPD increases, reaching a maximum removal of 25% of Zn. Moreover, Joule heating can complete the high-temperature treatment of samples within milliseconds. This extremely rapid heating and cooling process helps reduce the exposure time of samples to high temperatures, thereby minimizing oxidation and coarsening of the pore structure. The electrochemical active surface area of the porous copper samples prepared by Joule heating reaches a maximum of 317.6 times that of the original copper with a capacitance of 0.44 F (Fig. 10c). At a capacitance of 0.44 F, the VPD current collector achieved a maximum specific capacity of 435 mA h g^{-1} (Fig. 10a), 115.7% of the theoretical value of a graphite electrode, which exhibits superior performance compared to that of commercial copper foil. However, the rate performance of batteries utilizing VPD current collectors mostly fell short compared to those employing commercial copper foil (Fig. 10b).

The weight proportion of traditional metal-based current collectors in batteries is high, leading to an amount of reduction in energy density.[218] Hence, it is vital to develop thin films that possess stable properties, are lightweight, resistant to

corrosion, and exhibit high conductivity, serving as current collectors. Graphene is a promising material for current collectors due to its high conductivity, remarkable chemical stability, and lightweight properties.[219–223] Chen *et al.* fabricated a highly conductive reduced graphene oxide (RGO) film using a solution-based filtration process, followed by thermal reduction at 773 K and current-induced annealing (Joule heating at 2750 K for less than 1 minute) (Fig. 10d).[216] The high temperature generated by Joule heating effectively eliminates defects in graphene oxide (GO), promotes thermal reduction of GO and improves the crystal structure of individual RGO nanosheets, resulting in a highly crystalline graphene structure. A significant advantage of the Joule heating process is the extremely high local temperatures generated when current passes through areas of higher resistance, which not only promotes the reduction of GO but may also form cross-links at defect sites. It also leads to the highly stacked and densified structure of RGO nanosheets, facilitating the cross-linking of RGO layers, thereby achieving a record-breaking high direct current electrical conductivity (3112 S cm^{-1}) (Fig. 10e). This conductivity is significantly higher than that of RGO films prepared by chemical reduction or thermal reduction methods (usually less than 1000 S cm^{-1}). Moreover, the RGO film exhibits a low thickness of 4 μm, a low sheet resistance of 0.8 Ω sq^{-1}, excellent flexibility and a stable structure, making it suitable for use as an ultralight current collector.

To address the issue of poor physical contact between nanostructures, Yao *et al.* introduced a novel technique to construct a 3D interconnected carbon matrix through the formation of covalent bonds between carbon nanostructures.[217] The high temperature generated by Joule heating, with an ultrafast heating rate of 200 K min^{-1}, elevated the temperature of carbon nanofiber (CNF) films to above 2500 K. This high-temperature environment promotes the graphitization process, enabling the formation of highly crystalline carbon structures in a much shorter time than traditional furnace heating methods. Simultaneously, Joule heating causes welding of graphite carbon bonds between adjacent nanofibers, forming a continuous 3D carbon network (Fig. 10f and g). This 3D network improves physical contact between nanostructures, enhancing conductivity. The original electrical conductivity and sheet resistance of the pristine CNF film were 0.0133 S cm^{-1} and 18 400 Ω sq^{-1}, respectively. In contrast, the electrical conductivity of the carbon matrix after Joule heating treatment increased by four orders of magnitude to 380 S cm^{-1} (Fig. 10h), with a sheet resistance of 1.75 Ω sq^{-1}. The electrochemical performance and mechanical properties were significantly improved. Compared to traditional 2D planar current collectors, the 3D porous structure of the Joule-heated CNF film facilitates the penetration of cathode materials such as $LiFePO_4$, significantly reducing the electronic conduction distance during electrochemical reactions. This demonstrates the potential application of the Joule-heated CNF film as a current collector. Furthermore, the heating treatment of CNF films by the Joule heating method has the advantages of speed, high production efficiency, and low energy consumption.

4. Prospects for the future

Joule heating, as an energy-efficient and controllable heating method, demonstrates significant potential in the synthesis of energy storage materials and has broad application prospects. However, the application of this technology also faces several notable challenges, which currently lack targeted in-depth research. Addressing these challenges will be crucial for advancing Joule heating in energy storage applications.

(1) Localized overheating problems: during the Joule heating process, the current tends to flow along the path of least resistance, which can lead to localized overheating in certain areas of the material, thus affecting its uniformity and overall performance. This problem is particularly prominent in materials with uneven conductivity, such as composites. To address this problem, improvements can be made to the Joule heating apparatus by using patterned or layered electrode structures to optimize current distribution and employing multiple current inputs to achieve more uniform heating. Additionally, advanced control algorithms can be combined to dynamically adjust the current intensity and distribution, ensuring precise and uniform heating.

(2) Precise temperature control problems: Joule heating directly heats the material through current, raising its temperature to high levels within a very short time, resulting in an extremely rapid reaction process. The fast-heating rate can make precise temperature control challenging, especially when synthesizing high-precision materials or those with specific morphologies that require exact temperature control. Moreover, temperature fluctuations during the heating process can introduce new structural defects, affecting the material's electrochemical performance. Future research should incorporate high-sensitivity and fast-response temperature sensing technologies into the Joule heating system and develop feedback-based control systems. These systems should provide precise real-time temperature monitoring and automatically adjust the current to maintain the desired heating temperature.

(3) Scalability problems: Joule heating is currently primarily applied in small-scale laboratory research, where it shows great potential. However, achieving large-scale production remains challenging. Since Joule heating relies on the current flowing through the material to generate heat, processing large batches of samples requires high thermal conductivity of the materials. If the samples have low thermal conductivity, it can result in uneven temperature distribution, causing incomplete reactions in some parts and affecting the uniformity and performance of the samples. To solve this problem, further optimization of the Joule heating system is necessary. This can include combining it with other heating technologies, such as microwave heating or induction heating, to improve temperature uniformity when processing large quantities of materials. Additionally, adopting the modular heating unit design can ensure that each Joule heating unit can be independently controlled. This design allows for scalability by adding or reducing the number of heating units to maintain product consistency and performance.

(4) Safety problems: since Joule heating requires the use of high-power DC currents or large-capacity capacitors, it is essential to incorporate automatic power-off and alarm systems to promptly respond to electrical faults and reduce the risk of electric shock to operators. Flash Joule Heating is accompanied by intense bursts of blackbody radiation, thus, caution must be exercised to prevent the handling of flammable or explosive samples. Operators must wear standard-compliant protective eyewear and insulated gloves.

By addressing these challenges and exploring new research directions, the effectiveness and applicability of Joule heating technology in the preparation and application of energy storage materials will be significantly improved, bringing more possibilities to the development of energy storage technologies.

Now, the commercialization of large-scale production of high-quality turbostratic flash graphene (FG) has been achieved. The demonstration plant established by Universal Matter Inc in Canada commenced operations in the fourth quarter of 2023, achieving a graphene production capacity of 1 ton per day. Its highly advanced FJH process has successfully produced graphene with the highest purity grade. Although the FJH technology remains in the research and development phase, there is confidence that as the technology matures gradually, it will transition toward larger-scale commercialization.

5. Conclusion

This paper reviews the most recent advancements in energy storage research based on Joule heating, especially the current research status in the preparation of graphene and other 2D nanomaterials. Besides, this study provides a comprehensive overview and analysis of the utilization of this technology across diverse applications, including electrodes, supercapacitors, electrode material retrieval, solid-state electrolytes, and current collector treatment. The discussion encompasses different raw materials, process parameters, and material characteristics. The development and application of Joule heating offer fascinating benefits and chances in the field of energy storage, with plenty of space for expansion in the future. However, to promote the wider application and large-scale commercialization of this technology, close collaboration and relentless innovation between the scientific and industrial sectors are still required. Overcoming various limitations and challenges of Joule heating technique is essential to significantly contribute to advancing sustainable energy development and achieving global energy transition.

Author contributions

Jiahui Yuan: investigation, formal·analysis, writing – original draft. Yizi Zhang: data·curation, formal·analysis, writing – review & editing. Fuzhou Chen: writing – review & editing. Zhengrong Gu: supervision, writing – review & editing.

Data availability

No primary research results, software or code have been included and no new data were generated or analysed as part of this review.

Conflicts of interest

There are no conflicts to declare.

Acknowledgements

This work was supported by Sungrant USDA: USDA/NIFA, Advancing the Bioeconomy through Regional Sun Grant Centers, Production of 3D Graphene from Renewable Lignin Through Flash Catalytic Thermochemical Processes (SA2100372), and SD BOR pte SDSM&T, South Dakota Center for Electrochemical (SA2200071).

Notes and references

1 Y. Sun, C. Li, C. Yang, G. Dai, L. Li, Z. Hu, D. Wang, Y. Liang, Y. Li and Y. Wang, *Adv. Sci.*, 2022, **9**, 2103493.
2 E. Zhang, B. Wang, J. Wang, H. Ding, S. Zhang, H. Duan, X. Yu and B. Lu, *Chem. Eng. J.*, 2020, **389**, 124407.
3 J. Lee, H. Song, K. A. Min, Q. Guo, D. Kim, Z. Zheng, B. Han, Y. Jung and L. Y. S. Lee, *Small Methods*, 2021, **5**, 2100215.
4 N. Dunlap, D. B. Sulas-Kern, P. J. Weddle, F. Usseglio-Viretta, P. Walker, P. Todd, D. Boone, A. M. Colclasure, K. Smith and B. J. T. de Villers, *J. Power Sources*, 2022, **537**, 231464.
5 G. Xiong, Y. Chen, Z. Zhou, F. Liu, X. Liu, L. Yang, Q. Liu, Y. Sang, H. Liu and X. Zhang, *Adv. Funct. Mater.*, 2021, **31**, 2009580.
6 W. Chen, C. Ge, J. T. Li, J. L. Beckham, Z. Yuan, K. M. Wyss, P. A. Advincula, L. Eddy, C. Kittrell, J. Chen, D. X. Luong, R. A. Carter and J. M. Tour, *ACS Nano*, 2022, **16**, 6646–6656.
7 W. Zhu, H. Su, P. Bai, Z. Li, J. Zhang, J. Zhang, M. Li, Y. Chen and Y. Xu, *Chem. Eng. J.*, 2024, **480**, 148045.
8 Z. Liu, C. Duan, S. Dou, Q. Yuan, J. Xu, W. D. Liu and Y. Chen, *Small*, 2022, **18**, 2200954.
9 D. X. Luong, K. V. Bets, W. A. Algozeeb, M. G. Stanford, C. Kittrell, W. Chen, R. V. Salvatierra, M. Ren, E. A. McHugh, P. A. Advincula, Z. Wang, M. Bhatt, H. Guo, V. Mancevski, R. Shahsavari, B. I. Yakobson and J. M. Tour, *Nature*, 2020, **577**, 647–651.
10 J. Zhao, Z. Wang, X. Fang, L. Yang, C. Wu, W. Gan, Y. Zhou, L. Shan and Y. Lin, *J. Alloys Compd.*, 2023, **966**, 171535.
11 J. P. Joule, *London, Edinburgh Dublin Philos. Mag. J. Sci.*, 1845, **27**, 205–207.
12 J. P. Joule, *Abstracts of the Papers Communicated to the Royal Society of London*, 1843, vol. 5, p. 839.
13 B. Guralnik, O. Hansen, H. H. Henrichsen, B. Beltrán-Pitarch, F. W. Østerberg, L. Shiv, T. A. Marangoni, A. R. Stilling-Andersen, A. Cagliani and M. F. Hansen, *Rev. Sci. Instrum.*, 2021, **92**, 094711.

14 X. Xuan, *Electrophoresis*, 2008, **29**, 33–43.
15 R. K. Murakami and V. Villas-Boas, *Mater. Res.*, 1999, **2**, 67–73.
16 C. Wang, W. Ping, Q. Bai, H. Cui, R. Hensleigh, R. Wang, A. H. Brozena, Z. Xu, J. Dai and Y. Pei, *Science*, 2020, **368**, 521–526.
17 S. Yang, S. Yang, R. Pang, X. Zhao, L. Fan, M. Zhang and L. An, *Int. J. Appl. Ceram. Technol.*, 2023, **20**, 306–312.
18 E. Bichaud, J. M. Chaix, C. Carry, M. Kleitz and M. C. Steil, *J. Eur. Ceram. Soc.*, 2015, **35**, 2587–2592.
19 B. Deng, D. X. Luong, Z. Wang, C. Kittrell, E. A. McHugh and J. M. Tour, *Nat. Commun.*, 2021, **12**, 5794.
20 M. Cologna, B. Rashkova and R. Raj, *J. Am. Ceram. Soc.*, 2010, **93**, 3556–3559.
21 H. Xie, N. Liu, Q. Zhang, H. Zhong, L. Guo, X. Zhao, D. Li, S. Liu, Z. Huang and A. D. Lele, *Nature*, 2023, **623**, 964–971.
22 M. Saadi, P. A. Advincula, M. S. H. Thakur, A. Z. Khater, S. Saad, A. Shayesteh Zeraati, S. K. Nabil, A. Zinke, S. Roy and M. Lou, *Sci. Adv.*, 2022, **8**, eadd3555.
23 Z. Xue, J. Lu and H. Huang, *Diamond Relat. Mater.*, 2022, **128**, 109221.
24 D. Xia, J. Mannering, P. Huang, Y. Xu, Q. Li, H. Li, Y. Qin, A. N. Kulak and R. Menzel, *J. Am. Chem. Soc.*, 2024, **146**, 159–169.
25 S. Upama, A. Mikhalchan, L. Arevalo, M. Rana, A. Pendashteh, M. J. Green and J. J. Vilatela, *ACS Appl. Mater. Interfaces*, 2023, **15**, 5590–5599.
26 J. Zhang, J. Luo, Z. Guo, Z. Liu, C. Duan, S. Dou, Q. Yuan, P. Liu, K. Ji, C. Zeng, J. Xu, W. D. Liu, Y. Chen and W. Hu, *Adv. Energy Mater.*, 2022, **13**, 2203061.
27 Z. Sun and Y. H. Hu, *Angew. Chem., Int. Ed.*, 2020, **59**, 9232–9234.
28 W. Bao, A. D. Pickel, Q. Zhang, Y. Chen, Y. Yao, J. Wan, K. Fu, Y. Wang, J. Dai and H. Zhu, *Adv. Mater.*, 2016, 4684–4691.
29 M. Yi and Z. Shen, *J. Mater. Chem. A*, 2015, **3**, 11700–11715.
30 Y. Zhang, H. Lin, L. Zhang, S. Peng, Z. Weng, J. Wang, L. Wu and L. Zheng, *Appl. Surf. Sci.*, 2023, **611**, 155649.
31 S. Kataria, S. Wagner, J. Ruhkopf, A. Gahoi, H. Pandey, R. Bornemann, S. Vaziri, A. D. Smith, M. Ostling and M. C. Lemme, *Phys. Status Solidi A*, 2014, **211**, 2439–2449.
32 S. Xu, L. Zhang, B. Wang and R. S. Ruoff, *Cell Rep. Phys. Sci.*, 2021, **2**, 100372.
33 H. Song, X. Zhang, J. Ye, Y. Yang, D. Sun, C. Xu, R. Lin, X. Zhang, M. Zhang and S. Li, *Chem. Eng. Sci.*, 2023, **274**, 118706.
34 T. Kuila, A. K. Mishra, P. Khanra, N. H. Kim and J. H. Lee, *Nanoscale*, 2013, **5**, 52–71.
35 Y. Wang, G. Hu, Y. Cao, Z. Peng and K. Du, *Mater. Chem. Phys.*, 2021, **265**, 124523.
36 B. Mi, *Science*, 2019, **364**, 1033–1034.
37 W. S. Hummers Jr and R. E. Offeman, *J. Am. Chem. Soc.*, 1958, **80**, 1339.
38 M. Hirata, T. Gotou, S. Horiuchi, M. Fujiwara and M. Ohba, *Carbon*, 2004, **42**, 2929–2937.
39 M. Hirata, T. Gotou and M. Ohba, *Carbon*, 2005, **43**, 503–510.
40 L. Lin, B. Deng, J. Sun, H. Peng and Z. Liu, *Chem. Rev.*, 2018, **118**, 9281–9343.
41 X. Liu and H. Luo, *ACS Omega*, 2024, **9**, 2657–2663.
42 C. Zhou, Proceedings Volume 12600, International Conference on Optoelectronic Materials and Devices (ICOMD 2022), 2023, DOI: **10.1117/12.2674021**.
43 P. A. Advincula, D. X. Luong, W. Chen, S. Raghuraman, R. Shahsavari and J. M. Tour, *Carbon*, 2021, **178**, 649–656.
44 W. A. Algozeeb, P. E. Savas, D. X. Luong, W. Chen, C. Kittrell, M. Bhat, R. Shahsavari and J. M. Tour, *ACS Nano*, 2020, **14**, 15595–15604.
45 K. M. Wyss, J. L. Beckham, W. Chen, D. X. Luong, P. Hundi, S. Raghuraman, R. Shahsavari and J. M. Tour, *Carbon*, 2021, **174**, 430–438.
46 S. J. Barnes, *Environ. Pollut.*, 2019, **249**, 812–821.
47 A. K. Awasthi, M. Shivashankar and S. Majumder, *IOP Conf. Ser.: Mater. Sci. Eng.*, 2017, **263**, 022024.
48 S. Al-Salem, P. Lettieri and J. Baeyens, *Waste Manage.*, 2009, **29**, 2625–2643.
49 B. Deng, Z. Liu and H. Peng, *Adv. Mater.*, 2019, **31**, 1800996.
50 K. Parvez, S. Yang, X. Feng and K. Müllen, *Synth. Met.*, 2015, **210**, 123–132.
51 L. Liu, M. Qing, Y. Wang and S. Chen, *J. Mater. Sci. Technol.*, 2015, **31**, 599–606.
52 H. Wang, J. T. Robinson, X. Li and H. Dai, *J. Am. Chem. Soc.*, 2009, **131**, 9910–9911.
53 A. B. Kaiser, C. Gómez-Navarro, R. S. Sundaram, M. Burghard and K. Kern, *Nano Lett.*, 2009, **9**, 1787–1792.
54 C. Mattevi, G. Eda, S. Agnoli, S. Miller, K. A. Mkhoyan, O. Celik, D. Mastrogiovanni, G. Granozzi, E. Garfunkel and M. Chhowalla, *Adv. Funct. Mater.*, 2009, **19**, 2577–2583.
55 D. Voiry, J. Yang, J. Kupferberg, R. Fullon, C. Lee, H. Y. Jeong, H. S. Shin and M. Chhowalla, *Science*, 2016, **353**, 1413–1416.
56 Y. Li, H. Zhu, F. Shen, J. Wan, X. Han, J. Dai, H. Dai and L. Hu, *Adv. Funct. Mater.*, 2014, **24**, 7366–7372.
57 S. H. Noh, W. Eom, W. J. Lee, H. Park, S. B. Ambade, S. O. Kim and T. H. Han, *Carbon*, 2019, **142**, 230–237.
58 C. B. Kim, J. Lee, J. Cho and M. Goh, *Carbon*, 2018, **139**, 386–392.
59 R. Jakhar, J. E. Yap and R. Joshi, *Carbon*, 2020, **170**, 277–293.
60 R. Negishi, T. Nakagiri, M. Akabori and Y. Kobayashi, *Thin Solid Films*, 2023, **775**, 139841.
61 K. M. Wyss, D. X. Luong and J. M. Tour, *Adv. Mater.*, 2022, **34**, 2106970.
62 M. Chhowalla, H. S. Shin, G. Eda, L.-J. Li, K. P. Loh and H. Zhang, *Nat. Chem.*, 2013, **5**, 263–275.
63 T. Zhang, B. Jiang, Z. Xu, R. G. Mendes, Y. Xiao, L. Chen, L. Fang, T. Gemming, S. Chen and M. H. Rümmeli, *Nat. Commun.*, 2016, **7**, 13911.
64 M. Acerce, D. Voiry and M. Chhowalla, *Nat. Nanotechnol.*, 2015, **10**, 313–318.
65 F. Chen, C. Sun, S. J. Robertson, S. Chen, Y. Zhu, M. Shao and J. Wang, *Nano Energy*, 2022, **104**, 107894.

66 J. Huang, Z. Wei, J. Liao, W. Ni, C. Wang and J. Ma, *J. Energy Chem.*, 2019, **33**, 100–124.
67 X. Li, Z. Liu, D. Zhu, Y. Yan and Y. Chen, *Nanoscale*, 2022, **14**, 5869–5875.
68 M. S. Sokolikova and C. Mattevi, *Chem. Soc. Rev.*, 2020, **49**, 3952–3980.
69 W. Chen, Z. Wang, K. V. Bets, D. X. Luong, M. Ren, M. G. Stanford, E. A. McHugh, W. A. Algozeeb, H. Guo and G. Gao, *ACS Nano*, 2021, **15**, 1282–1290.
70 A. Ambrosi, Z. Sofer and M. Pumera, *Chem. Commun.*, 2015, **51**, 8450–8453.
71 D. Wang, X. Zhang, S. Bao, Z. Zhang, H. Fei and Z. Wu, *J. Mater. Chem. A*, 2017, **5**, 2681–2688.
72 N. Xuan, J. Chen, J. Shi, Y. Yue, P. Zhuang, K. Ba, Y. Sun, J. Shen, Y. Liu and B. Ge, *Chem. Mater.*, 2018, **31**, 429–435.
73 Z. Wu, C. Tang, P. Zhou, Z. Liu, Y. Xu, D. Wang and B. Fang, *J. Mater. Chem. A*, 2015, **3**, 13050–13056.
74 M. Kaur, K. Singh, A. Vij and A. Kumar, *New J. Chem.*, 2023, 2137–2160.
75 C. N. R. Rao and M. Chhetri, *Adv. Mater.*, 2019, **31**, 1803668.
76 D. Shi, B. Chang, Z. Ai, H. Jiang, F. Chen, Y. Shao, J. Shen, Y. Wu and X. Hao, *Nanoscale*, 2021, **13**, 2849–2854.
77 C. N. R. Rao and K. Gopalakrishnan, *ACS Appl. Mater. Interfaces*, 2017, **9**, 19478–19494.
78 S. Wang, F. Ma, H. Jiang, Y. Shao, Y. Wu and X. Hao, *ACS Appl. Mater. Interfaces*, 2018, **10**, 19588–19597.
79 D. Shi, M. Yang, B. Zhang, H. Hu, Z. Ai, Y. Shao, J. Shen, Y. Wu and X. Hao, *J. Colloid Interface Sci.*, 2022, **626**, 544–553.
80 M. G. Stanford, K. V. Bets, D. X. Luong, P. A. Advincula, W. Chen, J. T. Li, Z. Wang, E. A. McHugh, W. A. Algozeeb and B. I. Yakobson, *ACS Nano*, 2020, **14**, 13691–13699.
81 W. Chen, J. T. Li, Z. Wang, W. A. Algozeeb, D. X. Luong, C. Kittrell, E. A. McHugh, P. A. Advincula, K. M. Wyss and J. L. Beckham, *ACS Nano*, 2021, **15**, 11158–11167.
82 K. Ba, W. Jiang, J. Cheng, J. Bao, N. Xuan, Y. Sun, B. Liu, A. Xie, S. Wu and Z. Sun, *Sci. Rep.*, 2017, **7**, 45584.
83 L. Song, L. Ci, H. Lu, P. B. Sorokin, C. Jin, J. Ni, A. G. Kvashnin, D. G. Kvashnin, J. Lou and B. I. Yakobson, *Nano Lett.*, 2010, **10**, 3209–3215.
84 W. Chen, J. T. Li, C. Ge, Z. Yuan, W. A. Algozeeb, P. A. Advincula, G. Gao, J. Chen, K. Ling and C. H. Choi, *Adv. Mater.*, 2022, **34**, 2202666.
85 H. Li, R. Y. Tay, S. H. Tsang, L. Jing, M. Zhu, F. N. Leong and E. H. T. Teo, *RSC Adv.*, 2017, **7**, 12511–12517.
86 P. Giusto, D. Cruz, T. Heil, N. Tarakina, M. Patrini and M. Antonietti, *Adv. Sci.*, 2021, **8**, 2101602.
87 D. Chen, Y. Huang, X. Hu, R. Li, Y. Qian and D. Li, *Materials*, 2018, **11**, 387.
88 X. Zeng, H. Chen, X. He, H. Zhang, W. Fang, X. Du, W. Li, Z. Huang and L. Zhao, *Environ. Res.*, 2022, **207**, 112178.
89 S. Zeng, W. Feng, H. Luo, Y. Tan, Y. Wang, H. Zhang, T. Zhang and S. Peng, *Chem. Phys. Lett.*, 2017, **674**, 164–167.
90 T. Zhang, S. Zeng and G. Wen, *Mater. Lett.*, 2014, **132**, 277–280.
91 J. J. Vilatela and R. Marcilla, *Chem. Mater.*, 2015, **27**, 6901–6917.
92 A. Monreal-Bernal and J. J. Vilatela, *ChemPlusChem*, 2018, **83**, 285–293.
93 M. Rana, V. S. Avvaru, N. Boaretto, R. Marcilla, V. Etacheri and J. J. Vilatela, *J. Mater. Chem. A*, 2019, **7**, 26596–26606.
94 A. Moya, N. Kemnade, M. R. Osorio, A. Cherevan, D. Granados, D. Eder and J. J. Vilatela, *J. Mater. Chem. A*, 2017, **5**, 24695–24706.
95 M. Rana, N. Boaretto, A. Mikhalchan, M. Vila Santos, R. Marcilla and J. J. Vilatela, *ACS Appl. Energy Mater.*, 2021, **4**, 5668–5676.
96 N. Boaretto, J. Almenara, A. Mikhalchan, R. Marcilla and J. J. Vilatela, *ACS Appl. Energy Mater.*, 2019, **2**, 5889–5899.
97 D. Fejes and K. Hernádi, *Materials*, 2010, **3**, 2618–2642.
98 T. Maruyama, H. Kondo, R. Ghosh, A. Kozawa, S. Naritsuka, Y. Iizumi, T. Okazaki and S. Iijima, *Carbon*, 2016, **96**, 6–13.
99 R. Das, Z. Shahnavaz, M. E. Ali, M. M. Islam and S. B. Abd Hamid, *Nanoscale Res. Lett.*, 2016, **11**, 1–23.
100 J. P. Gore and A. Sane, *Flame synthesis of carbon nanotubes*, 2011.
101 S. Paul and S. Samdarshi, *New Carbon Mater.*, 2011, **26**, 85–88.
102 C. Ye, L. Zhao, S. Yang and X. Li, *Small*, 2023, **20**, e2309027.
103 M. Li, J. Lu, Z. Chen and K. Amine, *Adv. Mater.*, 2018, **30**, 1800561.
104 C.-Y. Wang, T. Liu, X.-G. Yang, S. Ge, N. V. Stanley, E. S. Rountree, Y. Leng and B. D. McCarthy, *Nature*, 2022, **611**, 485–490.
105 A. N. Singh, M. Islam, A. Meena, M. Faizan, D. Han, C. Bathula, A. Hajibabaei, R. Anand and K. W. Nam, *Adv. Funct. Mater.*, 2023, **33**, 2304617.
106 K. Sada, J. Darga and A. Manthiram, *Adv. Energy Mater.*, 2023, **13**, 2302321.
107 X. X. Luo, W. H. Li, H. J. Liang, H. X. Zhang, K. D. Du, X. T. Wang, X. F. Liu, J. P. Zhang and X. L. Wu, *Angew. Chem.*, 2022, **134**, e202117661.
108 Y. Zhao, P. Zhang, J. Liang, X. Xia, L. Ren, L. Song, W. Liu and X. Sun, *Energy Storage Mater.*, 2022, **47**, 424–433.
109 H. Tang, L. Duan, J. Liao, X. Sheng, J. Xu and X. Zhou, *Energy Storage Mater.*, 2023, **62**, 102935.
110 C. Yang, Y. Yao, S. He, H. Xie, E. Hitz and L. Hu, *Adv. Mater.*, 2017, **29**, 1702714.
111 L. Wang, G. L. Seah, Y. Li, W. H. Tu, W. Manalastas Jr, M. J. H. Reavley, E. W. Corcoran Jr, A. K. Usadi, Z. Du and S. Madhavi, *Adv. Mater. Interfaces*, 2022, **9**, 2200151.
112 S. Dong, Y. Song, M. Su, G. Wang, Y. Gao, K. Zhu and D. Cao, *Chem. Eng. J.*, 2024, **481**, 147988.
113 X. Li, F. Chen, B. Zhao, S. Zhang, X. Zheng, Y. Wang, X. Jin, C. Dai, J. Wang and J. Xie, *Nano-Micro Lett.*, 2023, **15**, 32.
114 W. Zhu, J. Zhang, J. Luo, C. Zeng, H. Su, J. Zhang, R. Liu, E. Hu, Y. Liu and W. D. Liu, *Adv. Mater.*, 2023, **35**, 2208974.
115 W.-B. Jung, H. Park, J.-S. Jang, D. Y. Kim, D. W. Kim, E. Lim, J. Y. Kim, S. Choi, J. Suk and Y. Kang, *ACS Nano*, 2021, **15**, 4235–4244.

116 F. Luo, T. Lyu, J. Liu, P. Guo, J. Chen, X. Feng, D. Wang and Z. Zheng, *J. Energy Chem.*, 2024, **92**, 404–413.
117 S. Dong, Y. Song, Y. Fang, G. Wang, Y. Gao, K. Zhu and D. Cao, *ACS Appl. Energy Mater.*, 2024, DOI: **10.1021/acsaem.3c02975**.
118 X. Shan, Y. Zhong, L. Huang, F. Cao, J. Xiang, Y. Zhang, Y. Xia, X. Xia, M. Chen and X. He, *J. Solid State Electrochem.*, 2023, **27**, 1391–1398.
119 F. Zhang, Y. Yao, J. Wan, D. Henderson, X. Zhang and L. Hu, *ACS Appl. Mater. Interfaces*, 2017, **9**, 391–397.
120 W.-B. Jung, Y. J. Hong, J. Yoon, S. Moon, S. Choi, J. Suk, O. B. Chae, M. Wu and H.-T. Jung, *Nano Express*, 2022, **3**, 025005.
121 A. Mohamed, S. Dong, M. Elhefnawey, G. Dong, Y. Gao, K. Zhu and D. Cao, *Chem. Phys. Lett.*, 2023, **815**, 140362.
122 S. Liu, B. Liu, M. Liu, J. Xiong, Y. Gao, B. Wang and Y. Hu, *Nanoscale*, 2024, **16**, 2531–2539.
123 H. Yang, L. Sun, S. Zhai, X. Wang, C. Liu, H. Wu and W. Deng, *ACS Appl. Nano Mater.*, 2023, **6**, 2450–2458.
124 C. Wang, D. Yang, S. Huang, Y. Qin, W. Zhang and X. Qiu, *Green Chem.*, 2022, **24**, 5941–5951.
125 D. Wang, X. Li, J. Wang, J. Yang, D. Geng, R. Li, M. Cai, T.-K. Sham and X. Sun, *J. Phys. Chem. C*, 2012, **116**, 22149–22156.
126 X. He, R. Li, J. Liu, Q. Liu, D. Song and J. Wang, *Chem. Eng. J.*, 2018, **334**, 1573–1583.
127 D. Zhou, Z. Cai, X. Lei, W. Tian, Y. Bi, Y. Jia, N. Han, T. Gao, Q. Zhang and Y. Kuang, *Adv. Energy Mater.*, 2018, **8**, 1701905.
128 X. Han, J. Li, J. Lu, S. Luo, J. Wan, B. Li, C. Hu and X. Cheng, *Nano Energy*, 2021, **86**, 106079.
129 Y. Yu, M. Xiang, J. Guo, C. Su, X. Liu, H. Bai, W. Bai and K. Duan, *J. Colloid Interface Sci.*, 2019, **555**, 64–71.
130 B. J. Kwon, F. Dogan, J. R. Jokisaari, B. Key, C. Kim, Y.-S. Liu, J. Guo, R. F. Klie and J. Cabana, *ACS Appl. Mater. Interfaces*, 2019, **11**, 3823–3833.
131 R. Wang, X. Chen, Z. Huang, J. Yang, F. Liu, M. Chu, T. Liu, C. Wang, W. Zhu and S. Li, *Nat. Commun.*, 2021, **12**, 3085.
132 S. Karthikeyan, B. Narenthiran, A. Sivanantham, L. D. Bhatlu and T. Maridurai, *Mater. Today: Proc.*, 2021, **46**, 3984–3988.
133 N. N. Loganathan, V. Perumal, B. R. Pandian, R. Atchudan, T. N. J. I. Edison and M. Ovinis, *J. Energy Storage*, 2022, **49**, 104149.
134 X. Jin, L. Song, H. Yang, C. Dai, Y. Xiao, X. Zhang, Y. Han, C. Bai, B. Lu and Q. Liu, *Energy Environ. Sci.*, 2021, **14**, 3075–3085.
135 W. Raza, F. Ali, N. Raza, Y. Luo, K.-H. Kim, J. Yang, S. Kumar, A. Mehmood and E. E. Kwon, *Nano Energy*, 2018, **52**, 441–473.
136 J. Yin, W. Zhang, N. A. Alhebshi, N. Salah and H. N. Alshareef, *Small Methods*, 2020, **4**, 1900853.
137 Z. Shang, X. An, H. Zhang, M. Shen, F. Baker, Y. Liu, L. Liu, J. Yang, H. Cao and Q. Xu, *Carbon*, 2020, **161**, 62–70.
138 J. Zhang, J. Luo, Z. Guo, Z. Liu, C. Duan, S. Dou, Q. Yuan, P. Liu, K. Ji and C. Zeng, *Adv. Energy Mater.*, 2023, **13**, 2203061.
139 S. Zhu, F. Zhang, H.-G. Lu, J. Sheng, L. Wang, S.-D. Li, G. Han and Y. Li, *ACS Mater. Lett.*, 2022, **4**, 1863–1871.
140 G. M. Karim, P. Dutta, A. Majumdar, A. Patra, S. K. Deb, S. Das, N. V. Dambhare, A. K. Rath and U. N. Maiti, *Carbon*, 2023, **203**, 191–201.
141 S. H. Noh, H. B. Lee, K. S. Lee, H. Lee and T. H. Han, *ACS Appl. Mater. Interfaces*, 2022, **14**, 29867–29877.
142 G. Wang, S.-K. Kim, M. C. Wang, T. Zhai, S. Munukutla, G. S. Girolami, P. J. Sempsrott, S. Nam, P. V. Braun and J. W. Lyding, *ACS Nano*, 2019, **14**, 632–639.
143 X. Zhang, G. Han and S. Zhu, *Small*, 2023, **20**, 2305406.
144 M. He, G. Wang, Y. Zhu, Y. Wang, F. Liu and S. Luo, *Carbon*, 2022, **186**, 215–226.
145 Y. Zhao, H. Liu, S. Li, P. Chen, S. Jiang, J. Liu and F. Meng, *Composites Commun.*, 2022, **34**, 101263.
146 S. Hou, W. Cheng and F. Guo, *Sustainable Mater. Technol.*, 2023, **35**, e00570.
147 H. B. Lee, G. K. Veerasubramani, K. S. Lee, H. Lee and T. H. Han, *Carbon*, 2022, **198**, 252–263.
148 X. Sun, S. Hou, L. Yuan and F. Guo, *Carbon Lett.*, 2022, **32**, 1745–1756.
149 J. G. Kang, G. Wang and S.-K. Kim, *Materials*, 2020, **13**, 5255.
150 S. Li, Y. Zhao, P. Shi, J. Zhou, J. Long, N. Cao, J. Liu and F. Meng, *Adv. Eng. Mater.*, 2023, **25**, 2300402.
151 D. Liu, Y. Liu, Y. Ding and B. Fan, *RSC Adv.*, 2022, **12**, 20866–20875.
152 M. Shang, J. Zhang, X. Liu, Y. Liu, S. Guo, S. Yu, S. Filatov and X. Yi, *Appl. Surf. Sci.*, 2021, **542**, 148697.
153 W. Yang, M. Ni, X. Ren, Y. Tian, N. Li, Y. Su and X. Zhang, *Curr. Opin. Colloid Interface Sci.*, 2015, **20**, 416–428.
154 S. W. Bokhari, A. H. Siddique, P. C. Sherrell, X. Yue, K. M. Karumbaiah, S. Wei, A. V. Ellis and W. Gao, *Energy Rep.*, 2020, **6**, 2768–2784.
155 M. B. Arvas, H. Gürsu, M. Gencten and Y. Sahin, *J. Energy Storage*, 2021, **35**, 102328.
156 W. Zhang, C. Xu, C. Ma, G. Li, Y. Wang, K. Zhang, F. Li, C. Liu, H. M. Cheng and Y. Du, *Adv. Mater.*, 2017, **29**, 1701677.
157 T. V. Pham, J. G. Kim, J. Y. Jung, J. H. Kim, H. Cho, T. H. Seo, H. Lee, N. D. Kim and M. J. Kim, *Adv. Funct. Mater.*, 2019, **29**, 1905511.
158 L. Zhang, T. Wang, T.-N. Gao, H. Xiong, R. Zhang, Z. Liu, S. Song, S. Dai and Z.-A. Qiao, *CCS Chem.*, 2021, **3**, 870–881.
159 E. Fan, L. Li, Z. Wang, J. Lin, Y. Huang, Y. Yao, R. Chen and F. Wu, *Chem. Rev.*, 2020, **120**, 7020–7063.
160 X. Hu, E. Mousa, Y. Tian and G. Ye, *J. Power Sources*, 2021, **483**, 228936.
161 S. Dong, Y. Song, K. Ye, J. Yan, G. Wang, K. Zhu and D. Cao, *EcoMat*, 2022, **4**, e12212.
162 S. Natarajan and V. Aravindan, *Adv. Energy Mater.*, 2020, **10**, 2002238.
163 Y. He, T. Zhang, F. Wang, G. Zhang, W. Zhang and J. Wang, *J. Cleaner Prod.*, 2017, **143**, 319–325.
164 X. Qu, H. Xie, X. Chen, Y. Tang, B. Zhang, P. Xing and H. Yin, *ACS Sustainable Chem. Eng.*, 2020, **8**, 6524–6532.

165 W. Wang, Y. Zhang, L. Zhang and S. Xu, *J. Cleaner Prod.*, 2020, **249**, 119340.
166 Y. Yao, M. Zhu, Z. Zhao, B. Tong, Y. Fan and Z. Hua, *ACS Sustainable Chem. Eng.*, 2018, **6**, 13611–13627.
167 Y. Lai, X. Zhu, J. Li, Q. Gou, M. Li, A. Xia, Y. Huang, X. Zhu and Q. Liao, *Chem. Eng. J.*, 2023, **457**, 141196.
168 G.-Q. Yu, M.-Z. Xie, Z.-H. Zheng, Z.-G. Wu, H.-L. Zhao and F.-Q. Liu, *Resour., Conserv. Recycl.*, 2023, **199**, 107267.
169 F. Luo, T. Lyu, D. Wang and Z. Zheng, *Green Chem.*, 2023, 8950–8969.
170 W. Chen, R. V. Salvatierra, J. T. Li, C. Kittrell, J. L. Beckham, K. M. Wyss, N. La, P. E. Savas, C. Ge, P. A. Advincula, P. Scotland, L. Eddy, B. Deng, Z. Yuan and J. M. Tour, *Adv. Mater.*, 2023, **35**, e2207303.
171 Z. Cheng, Z. Luo, H. Zhang, W. Zhang, W. Gao, Y. Zhang, L. Qie, Y. Yao, Y. Huang and K. K. Fu, *Carbon Energy*, 2023, **6**, e395.
172 Y.-C. Yin, C. Li, X. Hu, D. Zuo, L. Yang, L. Zhou, J. Yang and J. Wan, *ACS Energy Lett.*, 2023, **8**, 3005–3012.
173 X.-B. Cheng, C.-Z. Zhao, Y.-X. Yao, H. Liu and Q. Zhang, *Chem*, 2019, **5**, 74–96.
174 W. Zhao, J. Yi, P. He and H. Zhou, *Electrochem. Energy Rev.*, 2019, **2**, 574–605.
175 K. Takada, *J. Power Sources*, 2018, **394**, 74–85.
176 Y. Cui, J. Wan, Y. Ye, K. Liu, L.-Y. Chou and Y. Cui, *Nano Lett.*, 2020, **20**, 1686–1692.
177 L. Xu, J. Li, W. Deng, H. Shuai, S. Li, Z. Xu, J. Li, H. Hou, H. Peng, G. Zou and X. Ji, *Adv. Energy Mater.*, 2021, **11**, 2000648.
178 C. Wang, K. Fu, S. P. Kammampata, D. W. McOwen, A. J. Samson, L. Zhang, G. T. Hitz, A. M. Nolan, E. D. Wachsman and Y. Mo, *Chem. Rev.*, 2020, **120**, 4257–4300.
179 A. Manthiram, X. Yu and S. Wang, *Nat. Rev. Mater.*, 2017, **2**, 1–16.
180 Q. Zhao, S. Stalin, C.-Z. Zhao and L. A. Archer, *Nat. Rev. Mater.*, 2020, **5**, 229–252.
181 D. Zuo, L. Yang, Z. Zou, S. Li, Y. Feng, S. J. Harris, S. Shi and J. Wan, *Adv. Energy Mater.*, 2023, **13**, 2301540.
182 L. Shen, J. Yang, G. Liu, M. Avdeev and X. Yao, *Mater. Today Energy*, 2021, **20**, 100691.
183 H. Tian, S. Liu, L. Deng, L. Wang and L. Dai, *Energy Storage Mater.*, 2021, **39**, 232–238.
184 S. Woo and B. Kang, *J. Mater. Chem. A*, 2022, **10**, 23185–23194.
185 T. Okumura, S. Taminato, Y. Miyazaki, M. Kitamura, T. Saito, T. Takeuchi and H. Kobayashi, *ACS Appl. Energy Mater.*, 2020, **3**, 3220–3229.
186 Z. Jiang, S. Wang, X. Chen, W. Yang, X. Yao, X. Hu, Q. Han and H. Wang, *Adv. Mater.*, 2020, **32**, 1906221.
187 J. Lu and Y. Li, *J. Mater. Sci.: Mater. Electron.*, 2021, **32**, 9736–9754.
188 H. Huo, J. Liang, N. Zhao, X. Li, X. Lin, Y. Zhao, K. Adair, R. Li, X. Guo and X. Sun, *ACS Energy Lett.*, 2020, **5**, 2156–2164.
189 J.-F. Wu, W. K. Pang, V. K. Peterson, L. Wei and X. Guo, *ACS Appl. Mater. Interfaces*, 2017, **9**, 12461–12468.
190 B. Tao, C. Ren, H. Li, B. Liu, X. Jia, X. Dong, S. Zhang and H. Chang, *Adv. Funct. Mater.*, 2022, **32**, 2203551.
191 H. Liu, Y. Liang, C. Wang, D. Li, X. Yan, C. W. Nan and L. Z. Fan, *Adv. Mater.*, 2023, **35**, 2206013.
192 R. Wang, Q. Dong, C. Wang, M. Hong, J. Gao, H. Xie, M. Guo, W. Ping, X. Wang and S. He, *Adv. Mater.*, 2021, **33**, 2100726.
193 M. Hong, Q. Dong, H. Xie, X. Wang, A. H. Brozena, J. Gao, C. Wang, C. Chen, J. Rao and J. Luo, *Mater. Today*, 2021, **42**, 41–48.
194 R. Wang, W. Ping, C. Wang, Y. Liu, J. Gao, Q. Dong, X. Wang, Y. Mo and L. Hu, *Adv. Mater.*, 2020, **32**, 2005059.
195 A. Sazvar, H. Sarpoolaky and M. Golmohammad, *Solid State Ionics*, 2022, **386**, 116054.
196 V. Avila, B. Yoon, S. Ghose, R. Raj and L. M. Jesus, *J. Eur. Ceram. Soc.*, 2021, **41**, 4552–4557.
197 C. Wang, H. Xie, W. Ping, J. Dai, G. Feng, Y. Yao, S. He, J. Weaver, H. Wang and K. Gaskell, *Energy Storage Mater.*, 2019, **17**, 234–241.
198 P. Jiang, G. Du, Y. Shi, F. She, P. Guo, G. Qian, X. Lu, F. Xie and X. Lu, *Chem. Eng. J.*, 2023, **451**, 138771.
199 H. Zhang, R. Dubey, M. Inniger, F. Okur, R. Wullich, A. Parrilli, D. T. Karabay, A. Neels, K. V. Kravchyk and M. V. Kovalenko, *Cell Rep. Phys. Sci.*, 2023, **4**, 101473.
200 M. Hong, Q. Dong, H. Xie, B. C. Clifford, J. Qian, X. Wang, J. Luo and L. Hu, *ACS Energy Lett.*, 2021, **6**, 3753–3760.
201 A. Curcio, A. G. Sabato, M. Nuñez Eroles, J. C. Gonzalez-Rosillo, A. Morata, A. Tarancón and F. Ciucci, *ACS Appl. Energy Mater.*, 2022, **5**, 14466–14475.
202 F. Okur, H. Zhang, D. T. Karabay, K. Muench, A. Parrilli, A. Neels, W. Dachraoui, M. D. Rossell, C. Cancellieri and L. P. Jeurgens, *Adv. Energy Mater.*, 2023, **13**, 2203509.
203 P. B. Vandiver, O. Soffer, B. Klima and J. Svoboda, *Science*, 1989, **246**, 1002–1008.
204 J. Gao, W. Guo, H. Yang, F. Shen and X. Han, *The Proceedings of the 9th Frontier Academic Forum of Electrical Engineering*, Lecture Notes in Electrical Engineering, Springer, Singapore, 2021, vol. 743, pp. 435–441, DOI: 10.1007/978-981-33-6609-1_38.
205 E. Ramos, A. Browar, J. Roehling and J. Ye, *ACS Energy Lett.*, 2022, **7**, 3392–3400.
206 A. G. Nguyen, R. Verma, G. C. Song, J. Kim and C. J. Park, *Adv. Sci.*, 2023, **10**, 2207744.
207 P. Zhu, D. Gastol, J. Marshall, R. Sommerville, V. Goodship and E. Kendrick, *J. Power Sources*, 2021, **485**, 229321.
208 C. C. Wang, Y. C. Lin, K. F. Chiu, H. J. Leu and T. H. Ko, *ChemistrySelect*, 2017, **2**, 4419–4427.
209 M. J. Lain, J. Brandon and E. Kendrick, *Batteries*, 2019, **5**, 64.
210 B. Lin, Y. Wang, X. Hu, W. Zhang and H. Qin, *Mater. Sci. Eng., B*, 2024, **300**, 117085.
211 Y. Chen, H. Feng, Y. Wang, Z. Tang and D. Chua, *Mater. Lett.*, 2018, **226**, 8–12.
212 C. Xu, Q. Hao and D. Zhao, *Nano Res.*, 2016, **9**, 908–916.
213 A. Huang, Y. He, Y. Zhou, Y. Zhou, Y. Yang, J. Zhang, L. Luo, Q. Mao, D. Hou and J. Yang, *J. Mater. Sci.*, 2019, **54**, 949–973.

214 B. Q. Xie, C. J. Zhou, L. Sang, X. D. Ma and J. S. Zhang, *Chem. Eng. Process.*, 2021, **159**, 108213.
215 Y. Zheng, H. Niu, D. He, S. Wang, Y. Cai and S. Zhang, *Microporous Mesoporous Mater.*, 2019, **276**, 251–259.
216 Y. Chen, K. Fu, S. Zhu, W. Luo, Y. Wang, Y. Li, E. Hitz, Y. Yao, J. Dai, J. Wan, V. A. Danner, T. Li and L. Hu, *Nano Lett.*, 2016, **16**, 3616–3623.
217 Y. Yao, K. K. Fu, S. Zhu, J. Dai, Y. Wang, G. Pastel, Y. Chen, T. Li, C. Wang, T. Li and L. Hu, *Nano Lett.*, 2016, **16**, 7282–7289.
218 C. Zhang, R. Lyu, W. Lv, H. Li, W. Jiang, J. Li, S. Gu, G. Zhou, Z. Huang and Y. Zhang, *Adv. Mater.*, 2019, **31**, 1904991.
219 S. J. R. Prabakar, Y.-H. Hwang, E. G. Bae, D. K. Lee and M. Pyo, *Carbon*, 2013, **52**, 128–136.
220 Z. Bo, W. Zhu, W. Ma, Z. Wen, X. Shuai, J. Chen, J. Yan, Z. Wang, K. Cen and X. Feng, *Adv. Mater.*, 2013, **25**, 5799–5806.
221 W. Guo, C. Yu, S. Li, J. Yang, Z. Liu, C. Zhao, H. Huang, M. Zhang, X. Han and Y. Niu, *Small*, 2017, **13**, 1701288.
222 B. Fang, D. Chang, Z. Xu and C. Gao, *Adv. Mater.*, 2020, **32**, 1902664.
223 Y. Zhao, J. Yang, J. Ma, Q. Wu, W. Qian, Z. Wang, H. Zhang, D. He and S. Mu, *ACS Sustainable Chem. Eng.*, 2021, **9**, 8635–8641.